

# Tau condensation on DNA mediates microtubule attachment suggesting a mitotic role for centromere-localized tau

---

Received: 4 October 2024

---

Accepted: 11 December 2025

---

Published online: 07 January 2026

---

 Check for updates

---

Celine Park<sup>1,7</sup>, Jaehun Jung<sup>1,7</sup>, Yuri Hong<sup>2,6,7</sup>, Haeun Yoo<sup>1</sup>, Keunsang Yang<sup>1</sup>, Jaehyeon Shin<sup>1</sup>, Minsik Kim<sup>1</sup>, Chan Lim<sup>1</sup>, Ayoung Jeong<sup>1</sup>, Seokyun Hong<sup>1</sup>, Jun Young Baek<sup>1</sup>, Sang-Hyun Rah<sup>1</sup>, Chaelin Lee-Eom<sup>1</sup>, Minseok Seo<sup>3</sup>, Yoori Kim<sup>3,4</sup>, Jae-Hyung Jeon<sup>1</sup>, Jong-Bong Lee<sup>1,2</sup>, Dong Soo Hwang<sup>2,5</sup> ✉ & Min Ju Shon<sup>1,2</sup> ✉

Tau protein, traditionally recognized for stabilizing microtubules and forming pathological aggregates, has recently been observed to form condensates in various contexts. While its condensation with RNA has been well studied, the interaction between tau and DNA, along with its biological significance, remains less explored. Here, using single-molecule experiments, we find that tau binds stably to naked DNA at nanomolar concentrations, leading to the local co-condensation of tau and DNA. These tau condensates on DNA can also interface with microtubules, leveraging tau's known role in promoting microtubule growth and organization. The dynamic nature of these condensates facilitates the remodeling of the DNA–microtubule assembly. Interestingly, phosphorylated tau and nucleosomal DNA exhibit distinct capacities to form condensates and recruit microtubules. Furthermore, imaging of mitotic cells with endogenous or exogenous tau reveals its localization to centromeres, engaging mitotic spindles, whereas expression of phosphomimetic tau mutants (T231D/S235D and S262D) causes defects in chromosome alignment. Building on these observations, we speculate that tau may play a role in mitosis, where tau clusters facilitate the early registration of mitotic spindles to chromosomes before kinetochore-mediated attachment. We also discuss the implications of this model in conditions where abnormal cell cycle re-entry and tau activity may disrupt cell division.

Tau protein has long been known for its primary role in stabilizing axonal microtubules in neurons<sup>1,2</sup>. More recently, its ability to facilitate the nucleation and growth of microtubules has gained attention<sup>3</sup>. This function relies on tau's tendency to form condensates at high concentrations<sup>4–7</sup>, a mechanism increasingly recognized as an organizing principle in many areas of cell biology<sup>8,9</sup>. At the same time, tau has been a major focus of research in neurodegenerative diseases due to its critical involvement in forming pathological aggregates<sup>10</sup>. The

abnormal aggregation of tau is a hallmark of tauopathies, including Alzheimer's disease, and is strongly associated with neuronal dysfunction and cell death.

In addition to binding microtubules, tau's multifaceted biophysical properties enable a variety of dynamic interactions<sup>11</sup>. As an intrinsically disordered protein with distinct domains<sup>12</sup>, tau adopts flexible conformations, allowing for weak multivalent interactions with both itself and other molecules. This ability is crucial for driving the

co-condensation of other factors within tau condensates. One example is tubulin, which has been shown to be recruited and to locally nucleate microtubule growth<sup>3</sup>. Another is the complexation between tau and RNA, which has been explored in the context of electrostatic interactions<sup>4,13</sup>, participation in stress granules<sup>14</sup>, and the development of tau fibrils and aggregates<sup>5,15,16</sup>. As a corollary, the interactions between tau, tubulin, and RNA can also modulate tau's ability to organize microtubules<sup>17</sup>. These examples suggest that tau condensates may act as hubs for various biomolecules sparking distinct cellular activities.

Unlike tau–RNA interactions, the interaction between tau and DNA has received less attention. Since tau primarily resides in the cytoplasm, its limited access to nuclear DNA may have reduced the perceived physiological relevance of tau–DNA binding. Nevertheless, interactions between tau and naked DNA molecules have been reported<sup>18–25</sup>, albeit infrequently. A recent biophysical investigation by Abasi *et al.* demonstrated that tau can co-condense with naked DNA and nucleosome arrays under low-salt conditions<sup>25</sup>, which can be disrupted by aberrant hyperphosphorylation of tau. While it is plausible that tau, having a net positive charge of  $-6$ , may bind dsDNA via electrostatic interactions similar to its RNA binding, the intrinsic stiffness of dsDNA likely renders tau–DNA interactions distinct. The biophysical strength of this interaction, as well as its potential role in living cells, remains largely unexplored. One notable exception is tau's role in the nucleus, where it has been proposed to protect the genome and influence gene expression<sup>26–28</sup>.

Here, we report that tau directly interacts with DNA, forming co-condensates that serve as dynamic platforms for microtubule organization. Our single-molecule observations reveal that 2N4R tau, the longest isoform of tau expressed in the adult human brain, forms mobile condensates on DNA strands at low concentrations. These tau–DNA co-condensates act as dynamic microtubule attachment sites, assembling microtubules around the DNA, with tau phosphorylation and nucleosomes adding further complexity to this process. Furthermore, by imaging tau-expressing cells during division, we observed tau clustering around the centromeres of mitotic chromosomes during prometaphase, poised to interface with nascent mitotic spindles. Expression of phosphomimetic tau variants in cells also resulted in the failure of some chromosomes to align at the metaphase plate. Based on these findings, we speculate a mitotic function of tau in tau-expressing cells such as neurons. We hypothesize that as the nuclear envelope breaks down and chromosomes become exposed to cytoplasmic tau, the dynamic rearrangement of tau on mitotic chromosomes facilitates the “search and

capture” process<sup>29</sup> of newly forming microtubules, a process traditionally considered random. This model further proposes that as tau–DNA co-condensates mature and migrate toward the centromeres, these transient attachment sites are gradually replaced by kinetochores for a more stable connection.

## Results

### Tau stably binds to naked DNA at nanomolar concentrations

To probe the interaction between tau protein (2N4R, tau-441) and naked DNA, we first examined the mobility of DNA in an agarose gel after mixing it with purified tau protein (Supplementary Fig. 1). The prepared dsDNA samples of varying lengths (24–5000 bp) all displayed a significant mobility shift when incubated with wild-type tau (500 nM or higher) (Supplementary Fig. 2), indicating a strong association between tau and DNA. This interaction was further enhanced when the NaCl concentration was lowered from 100 mM to 25 mM, suggesting an electrostatic nature of the binding, similar to tau–RNA complexation<sup>4</sup>. Given that the shortest DNA we prepared (24 bp) allowed tau binding, it is likely that the longer DNA constructs can accommodate proportionally more tau molecules along their length. A recent report on tau's phase separation behavior with naked DNA<sup>25</sup> is in quantitative agreement with our results.

While this bulk assay confirmed tau's DNA-binding properties, it did not reveal the distribution of tau within and across DNA strands, as well as the impact of this binding on DNA conformation. To address these questions, we set up a series of single-molecule imaging experiments that directly visualize the binding of tau protein to DNA substrates. We first performed a classic flow-stretching experiment in a flow chamber, where 48.5-kb  $\lambda$ -DNA molecules were attached to a polyethylene glycol (PEG)-coated glass coverslip by one end and then stretched upon buffer flow ( $7 \mu\text{L min}^{-1}$ ) (Fig. 1A). The stretched DNA strands were visualized using a fluorescent stain (SYTOX Orange) on a total internal reflection fluorescence (TIRF) microscope (Fig. 1B). The tethered  $\lambda$ -DNA molecules were gently stretched to  $6.2 \pm 0.6 \mu\text{m}$  ( $\sim 40\%$  of the contour length) (Fig. 1C, D), indicating  $\sim 0.1$  pN of flow-induced stretching force. When 500 nM tau (10% labeled with Cy5) was added at the same flow rate, the  $\lambda$ -DNA molecules gradually shortened and collapsed onto the attachment point (Fig. 1B–D and Supplementary Movie 1). We checked that the fluorescently labeled tau also accumulated on the condensed DNA spots (Fig. 1B, E), indicating that tau binding is the direct cause of DNA compaction. Note that these observations were made without highly concentrated tau solutions or

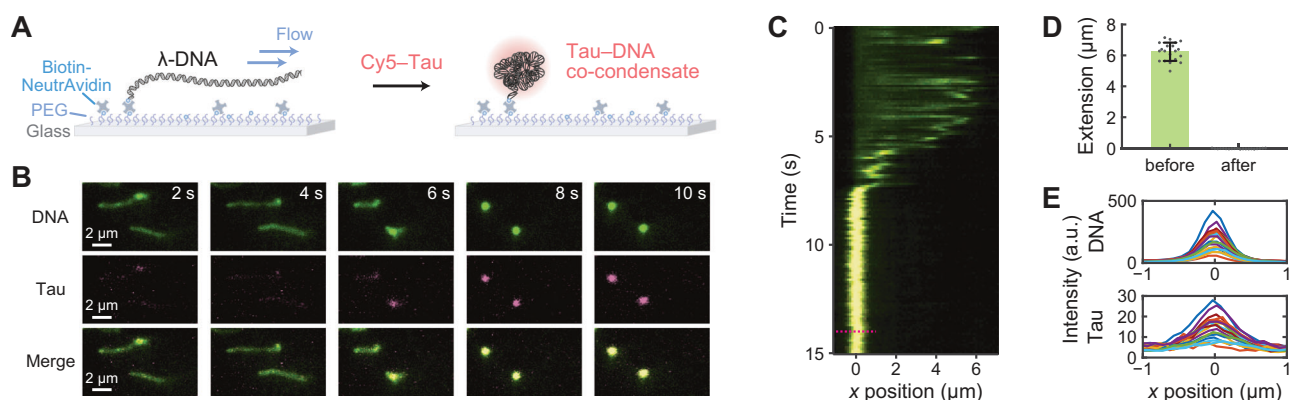


**Fig. 1 | Condensation of DNA by tau.** **A** Flow stretching of surface-tethered  $\lambda$ -DNA on polyethylene glycol (PEG)-coated glass, followed by the formation of tau–DNA co-condensates upon the addition of Cy5-labeled tau. **B** Time-lapse images from TIRF microscopy showing the co-condensation event during the addition of 500 nM tau. DNA is stained with SYTOX Orange (green), and tau is labeled with Cy5 (magenta). **C** Representative kymograph of the co-condensation event. The magenta dotted line indicates the region from which the fluorescence intensity

profiles were sampled, as shown in (E). **D** Extension of flow-stretched  $\lambda$ -DNA before and after tau addition ( $n = 20$  molecules; mean  $\pm$  s.d.). **E** Fluorescence intensity profiles (in arbitrary units) of DNA (top) and tau (bottom) after tau addition, sampled from multiple locations along the DNA and aligned to their respective attachment points ( $n = 20$  molecules). The colocalization of tau and DNA fluorescence indicates the formation of co-condensates.

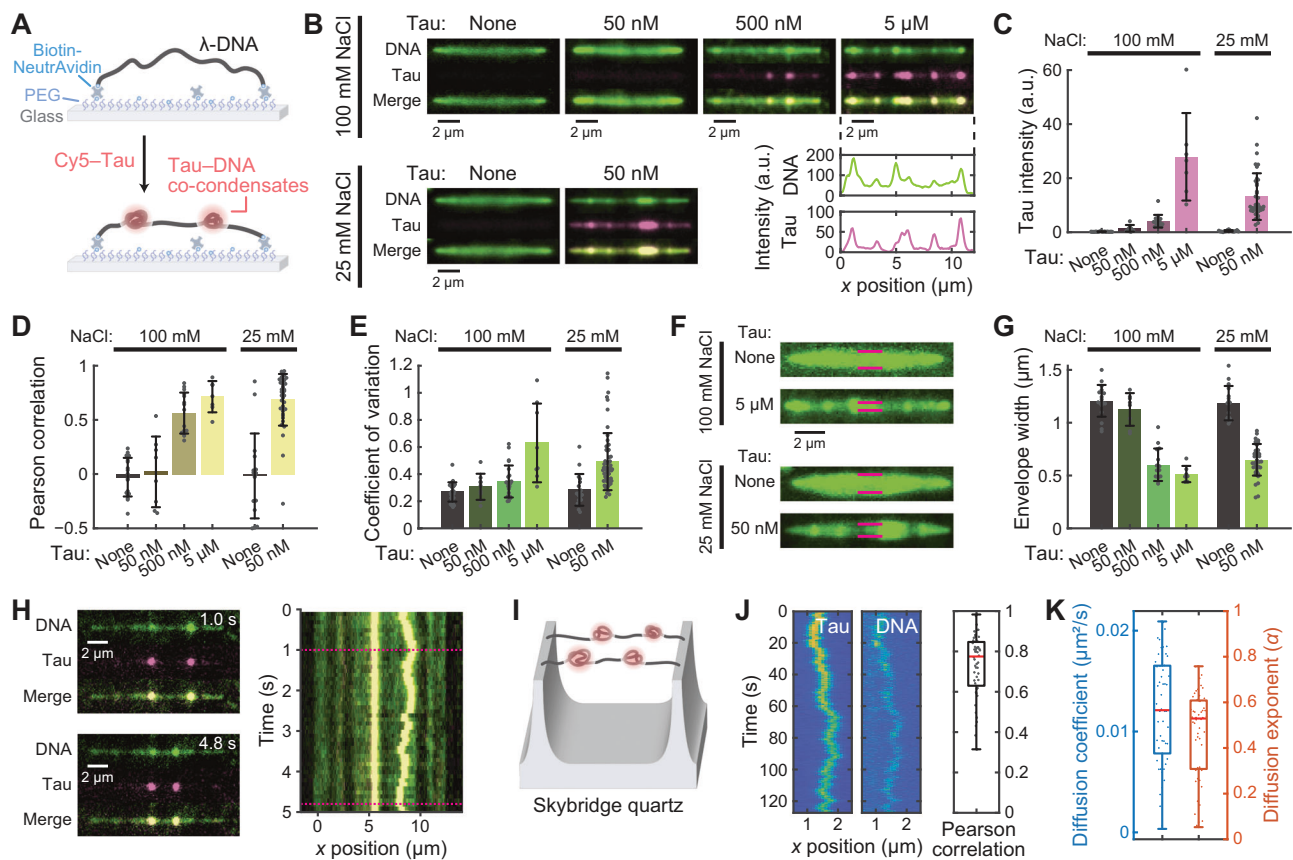


**Fig. 2 | Fluorescence imaging of tau–DNA co-condensates on DNA strands.**

**A** Schematic of tau–DNA co-condensation on doubly tethered  $\lambda$ -DNA on polyethylene glycol (PEG)-coated glass. **B** TIRF images of  $\lambda$ -DNA with different tau concentrations at 100 mM and 25 mM NaCl. DNA is labeled with SYTOX Orange (green), and tau with Cy5 (magenta). Intensity profiles (in arbitrary units) for 5  $\mu$ M tau (bottom right) high correlation between DNA and tau. **C** Quantification of tau fluorescence intensity for the conditions shown in (B). **D** Pearson correlation coefficients between DNA and tau fluorescence, indicating colocalization. **E** Coefficient of variation of DNA fluorescence images, reflecting the extent of DNA puncta formation induced by tau. **F** Maximum intensity projections of DNA fluctuations (over 5 s), showing the effect of tau on DNA flexibility. Magenta lines indicate the measured envelope width. **G** Distribution of DNA envelope width as a

function of tau and NaCl concentrations, reflecting changes in DNA tension. Data in (C–G) were obtained from the following sample sizes: for 100 mM NaCl,  $n = 27, 9, 23,$  and  $8$ ; and for 25 mM NaCl,  $n = 18$  and  $57$  (mean  $\pm$  s.d.). **H** Snapshots and kymograph of mobile tau–DNA co-condensates. Magenta dotted lines indicate snapshot locations. These images show that tau and DNA move together, indicating the mobility of the co-condensates. **I** Schematic of the DNA skybridge technique for visualizing condensate mobility. **J** Kymograph of tau and DNA movement obtained from the skybridge experiments, with a corresponding Pearson correlation plot. **K** Diffusion coefficients and exponents of tau–DNA co-condensates. Data in (J, K) are from  $n = 75$  spots that showed tau–DNA colocalization and diffusive behavior ( $\alpha > 0.05$ ); box plots show the median (red line) and interquartile range, with whiskers extending to the minimum and maximum values not considered outliers.

a crowding agent, both of which are typically needed to induce condensation behavior through liquid–liquid phase separation (LLPS)<sup>5,6,25,30</sup>. This indicates that a stable interaction between tau and naked DNA at nanomolar concentrations, which locally enriches tau, is sufficient to induce DNA compaction prior to the onset of LLPS-dependent tau–DNA co-condensation<sup>25</sup>.

### Tau binding to DNA generates local co-condensates

Recent discoveries indicate that DNA-binding proteins can form condensates on DNA, thereby compacting and remodeling the underlying structure<sup>31–37</sup>. Motivated by these findings, we hypothesized that tau could exert similar effects on DNA. To test this, we prepared  $\lambda$ -DNA molecules tethered at both ends to a surface and introduced Cy5-labeled tau again (Fig. 2A), simultaneously imaging the fluorescence of both tau and DNA. As observed in single-tether experiments, there was significant fluorescence from tau binding to the DNA (Fig. 2B, C, and Supplementary Movie 2). The DNA backbone was diffusely coated with tau, interspersed with multiple bright foci of  $\sim 1 \mu$ m or smaller, as revealed by the intensity profile cross section (Fig. 2B, inset). As expected from the bulk gel shift assay, tau binding was both tau and

salt concentration-dependent (Fig. 2C). Higher concentrations of tau resulted in more intense spots, even though we kept the concentration of the Cy5-labeled tau constant (50 nM) across all samples.

Although the DNA coverage by tau varied among DNA strands due to different levels of foci formation, the locations of these bright regions corresponded closely between DNA and tau signals (Fig. 2B inset and Fig. 2D), suggesting that clustered tau binding leads to local compaction of DNA. The level of local compaction was estimated by the coefficient of variation of the DNA fluorescence signal (the standard deviation of pixel intensities divided by their mean), which increased progressively as more tau was added (Fig. 2E). In contrast, DNA strands without tau showed uniform fluorescence along their length. Consistent with the local compaction effect, the binding of tau noticeably reduced the thermal fluctuation of DNA (Fig. 2F and Supplementary Movie 2), indicating that the DNA became shorter and tauter. The mean envelope width, or the amplitude of off-axis deviation due to fluctuation, gradually decreased as tau concentration increased from 50 nM to 5  $\mu$ M (Fig. 2G), consistent with the increase in tau binding. Notably, even 50 nM tau was sufficient to induce strong condensation of DNA under low-salt conditions (25 mM NaCl), as

demonstrated by both foci formation (Fig. 2B, E) and reduced fluctuation (Fig. 2G). Importantly, these findings were confirmed under 150 mM NaCl, which more closely approximates physiological salt conditions (Supplementary Fig. 3). These results demonstrate that wild-type tau protein at nano- to micromolar concentrations can stably bind to naked DNA under physiological conditions, consistent with the behavior reported by Abasi et al.<sup>25</sup>.

To ensure our findings on tau–DNA co-condensation extend beyond single-molecule observations, we checked bulk phase separation and subsequent co-condensation of high tau concentrations with dsDNA in the presence of 10% PEG, a standard crowding agent to drive LLPS. Under these conditions, tau and DNA readily formed co-condensates across various concentrations of tau, DNA, and salt (Supplementary Fig. 4), again consistent with the previous results<sup>25</sup>. Importantly, the co-condensation behavior was robust across a wide range of DNA lengths, from 24 bp to  $\lambda$ -DNA, indicating that DNA length did not significantly influence its partitioning into tau droplets. This tau-driven DNA condensation, reversing the above single-molecule observations of DNA-driven tau condensation, reinforces the strong molecular interaction between tau and DNA.

### Tau condensates slide along DNA to compact local segments

Surprisingly, despite the fast accumulation of tau on DNA (Fig. 1B), many of the tau condensates remained mobile along the DNA substrates (Fig. 2H and Supplementary Movie 3). Moreover, the location of DNA foci also followed tau movement across all tau concentrations we tested (50 nM–5  $\mu$ M). This suggests that tau clusters can slide along DNA to dynamically remodel the underlying segments, reminiscent of other LLPS-driven protein–DNA co-condensates. However, not all condensates exhibited uniform mobility, likely due to heterogeneity in their mechanical properties (e.g., differential maturation to more solid-like states), friction from contact with the PEG-coated glass surface, or a combination of both. To probe the internal dynamics of tau clusters, we performed fluorescence recovery after photobleaching (FRAP) on tau clusters assembled with 5  $\mu$ M tau along double-tethered  $\lambda$ -DNA (Supplementary Fig. 5). Bleaching and monitoring of tau fluorescence (Cy5) recovery yielded highly heterogeneous traces, reflecting frequent condensate movement, merging, and splitting, yet many traces exhibited substantial fluorescence return. A single-exponential fit of the mean recovery for representative traces gave a time constant of ~30 min and a mobile fraction of ~82%. However, these values represent a composite of fast- and slow-recovering populations and are affected by the loss of some condensates during monitoring. Overall, these results confirm that DNA-bound tau exchanges dynamically with the bulk pool in a liquid-like manner.

To alleviate the surface-imposed friction, we re-evaluated the mobility of tau–DNA condensates on the DNA skybridge platform (Fig. 2I)<sup>38</sup>. In this technique,  $\lambda$ -DNA is suspended between micro-fabricated quartz barriers, reducing surface interaction artifacts and enabling high-throughput visualization of condensate mobility. Indeed, by allowing sufficient spacing between the DNA strands and the substrate surface, we confirmed that the tau and DNA foci migrated together along the DNA strands (Fig. 2J and Supplementary Movie 4). Essentially all of the observed co-condensates ( $n=52$ ) showed sub-diffusive behavior, with an anomalous exponent ( $\alpha$ ) centered around 0.5 and diffusion coefficients of 0.01–0.02  $\mu\text{m}^2 \text{s}^{-1}$  (Fig. 2K), indicating transient confinement and the need to reorganize or drag compacted DNA segments as they slide along the polymer. The skybridge platform further provided a convenient means to probe the sequence preference of tau condensate localization (Supplementary Fig. 6). Condensates were observed more frequently in the AT-rich half of  $\lambda$ -DNA, consistent with tau's known preference for AT-rich sequences<sup>39</sup>, although the overall broad distribution reflects its predominantly nonspecific binding. In conclusion, these findings indicate that tau binding to DNA leads to dynamic co-

condensation, which spatiotemporally modulates the local compaction of DNA.

### Tau binding exerts piconewton condensation force on DNA

The flow-stretching and double-tether experiments showed that tau binding can induce DNA condensation, counteracting a force of at least ~0.1 pN from the buffer flow. We next employed magnetic tweezers to accurately measure the force generated by tau condensates on DNA and to determine if the condensation can be mechanically reversed (Fig. 3A). A 10-kb dsDNA fragment was prepared as a substrate, with one end attached to a PEG-coated glass surface and the other to a magnetic bead for manipulation. Changes in DNA extension were monitored by tracking the vertical movements of the bead. This setup was also equipped with a TIRF microscopy module<sup>40</sup>, which checked the fluorescence signal from tau molecules binding to DNA (Supplementary Fig. 7).

In the absence of tau, the classic worm-like-chain extension of dsDNA was reproduced by applying a force ramp between 0.1 and 10 pN (Fig. 3B, *left*). To ensure that the DNA constructs were free of single-stranded nicks, we used only those that collapsed under applied torque, exhibiting supercoiling behavior (Supplementary Fig. 7). However, when 500 nM tau was added to the buffer, the overall extension of DNA was notably reduced, especially in the low-force range between 0.1 and 3 pN (Fig. 3B, *center*), consistent with tau-induced condensation of DNA. Fluorescence verification confirmed the accumulation of tau molecules on the DNA strands (Supplementary Fig. 7, Supplementary Movie 5). At higher forces, in contrast, the extension returned fully to that of naked dsDNA, implying that the tau molecules were largely displaced by stretching the DNA. It was possible to drive this compaction and decompaction cycle by repeatedly stretching and relaxing the DNA. Although the exact force levels at which these transitions occurred varied across trials (Fig. 3C), slightly higher forces (1–3 pN) were required than those at which condensation first occurred (<1 pN), suggesting some mechanical hysteresis and energy dissipation in the tau–DNA interactions. Finally, increasing the concentration of tau (from 500 nM to 5  $\mu$ M) raised both condensation and decondensation forces, consistent with an increased tendency to undergo condensation.

### Tau–DNA co-condensation is cooperative

The force-extension curves in the presence of tau revealed both smooth and stepwise changes in DNA extension. We considered whether the stepwise changes might represent a specific unit length of DNA compacted by tau condensates of relatively uniform size. To better resolve these events, we applied force-jump cycles (Fig. 3D), where the force was abruptly switched between 0.5 and 3 pN to trigger compaction and decompaction events. During the stretching phase, we detected many stepwise length changes (Fig. 3E), with a median size of 72 nm (Fig. 3F). This stepwise unbinding reflects the cooperative nature of the tau–DNA condensates, as each step likely corresponds to the concerted rupture of a sub-domain held together by multivalent tau–tau and tau–DNA interactions.

To test this interpretation at the molecular level, we performed MD simulations of tau–DNA co-condensation under applied force (Supplementary Fig. 8). Here, ionic effects at physiological monovalent salt (~100 mM) were implicitly captured by setting the DNA persistence length to ~50 nm, which subsumes short-scale bending and salt-dependent flexibility (see Supplementary Note 1, “Molecular dynamics simulation for tau–DNA co-condensates” for more details). In silico, tau and DNA coalesce into droplets featuring looped DNA segments and characteristic bending, without strict periodicity (Fig. 3G). Simulated force–extension profiles recapitulated the experimentally observed stepwise jumps (Fig. 3H), and inspection of snapshots and local DNA densities before versus after individual jumps confirmed that each event corresponds to the rupture of a compacted DNA

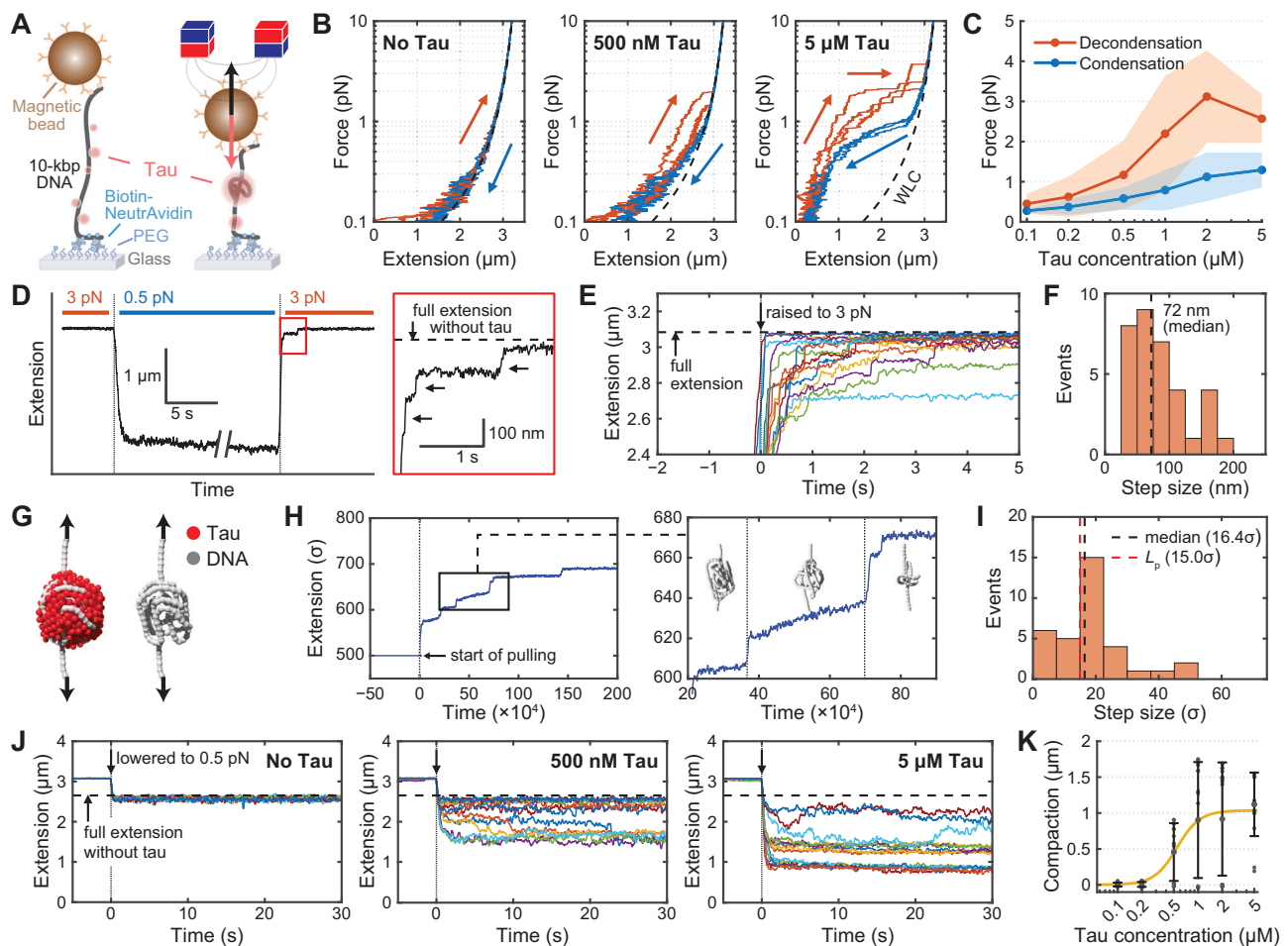


**Fig. 3 | Mechanics of tau-DNA co-condensation.** **A** Schematic of magnetic tweezers experiments to probe tau-DNA co-condensation. PEG: polyethylene glycol. **B** Representative force-extension curves of DNA during stretching (*orange*) and relaxation (*blue*) in the absence and presence of tau ( $n = 3$  cycles each). Dashed line shows the worm-like chain (WLC) model for dsDNA. **C** Condensation and decondensation forces obtained from force-extension measurements ( $n = 15$  events at each force; mean  $\pm$  s.d.), as shown in **(B)**. **D** Representative DNA extension trace under a force-jump protocol with  $5 \mu\text{M}$  tau, cycling between  $0.5 \text{ pN}$  (compaction) and  $3 \text{ pN}$  (stretching). Red box is expanded on the right to highlight stepwise jumps. **E** Extension trace with  $5 \mu\text{M}$  tau at  $3 \text{ pN}$  ( $n = 15$  trials), aligned at the force jump. **F** Step size histogram from **(E)** ( $n = 34$  events). **G–I** Coarse-grained simulation of stretching tau-DNA co-condensates. **G** Representative snapshot of a tau-DNA

co-condensate captured before force application. The right image shows DNA alone in the same configuration for clarity. **(H)** DNA extension during force-induced decondensation. Right, zoomed-in views of the boxed region, with snapshots of the DNA conformation before and after each stepwise jump. **I** Histograms of step sizes for extension events. The persistence length of dsDNA ( $L_p$ ) is indicated by the red dashed line for reference. **J** DNA extension at  $0.5 \text{ pN}$  measured by magnetic tweezers for different tau concentrations ( $n = 15$  trials each). **K** Compaction length of DNA under  $0.5 \text{ pN}$  force clamp as a function of tau concentration. Black dots represent individual condensation events ( $n = 15$  per concentration; mean  $\pm$  s.d.). The solid line represents a Hill equation fit, yielding a Hill coefficient of  $3.1 \pm 2.5$  and an apparent  $K_d$  of  $0.55 \pm 0.14 \mu\text{M}$  (values  $\pm$  95% confidence intervals).

domain (Supplementary Fig. 8). Importantly, the distribution of simulated step sizes peaked near the DNA persistence length (Fig. 3I), demonstrating that DNA bending rigidity defines the natural rupture unit. In contrast, simulations lacking bending energy (*i.e.*, a freely jointed chain model) produced much smaller, irregular steps (Supplementary Fig. 8).

During the condensation measurements under a constant  $0.5 \text{ pN}$  load, individual DNA tethers showed a binary response (Fig. 3J): they either collapsed rapidly into a condensed state (occasionally via discrete, slower steps) or remained fully extended, with large fluctuations over 1 min. Both the switch-like collapse and the slower fluctuations likely stem from cooperative tau condensation: rapid compaction follows cluster formation, while the larger, slower changes reflect cluster-mediated remodeling. To quantify this cooperativity, we measured the extent of DNA shortening as a function of tau concentration and observed a sharp transition near  $500 \text{ nM}$  (Fig. 3K). A Hill-plot analysis yielded a Hill coefficient of  $n = 3.1 \pm 2.5$  and an apparent  $K_d = 0.55 \pm 0.14 \mu\text{M}$  (95% confidence interval), reinforcing the

conclusion that multiple tau molecules bind DNA cooperatively with a moderate-to-high affinity.

### Tau condensates facilitate microtubule attachment to DNA

The tau condensates formed on DNA substrates are reminiscent of those that facilitate microtubule growth and assembly<sup>3</sup>. Presumably, the DNA-bound tau condensates might function similarly to organize microtubules, possibly by cooperating with tau molecules already present on the microtubule surface. To test this idea, we introduced a mixture of tau and tubulin over the surface-bound tau-DNA assembly and evaluated whether the tau condensates maintain their potential to organize a microtubule network. We first checked that mixing tubulin with tau in the presence of GTP and 5% PEG induced rapid polymerization of microtubules (Supplementary Fig. 9). When this solution of nascent microtubules was introduced over surface-tethered DNA molecules prepared at a low density, tau-DNA co-condensates effectively captured them (Fig. 4), suggesting that tau retains its essential microtubule binding activity. Importantly, fluorescence from free

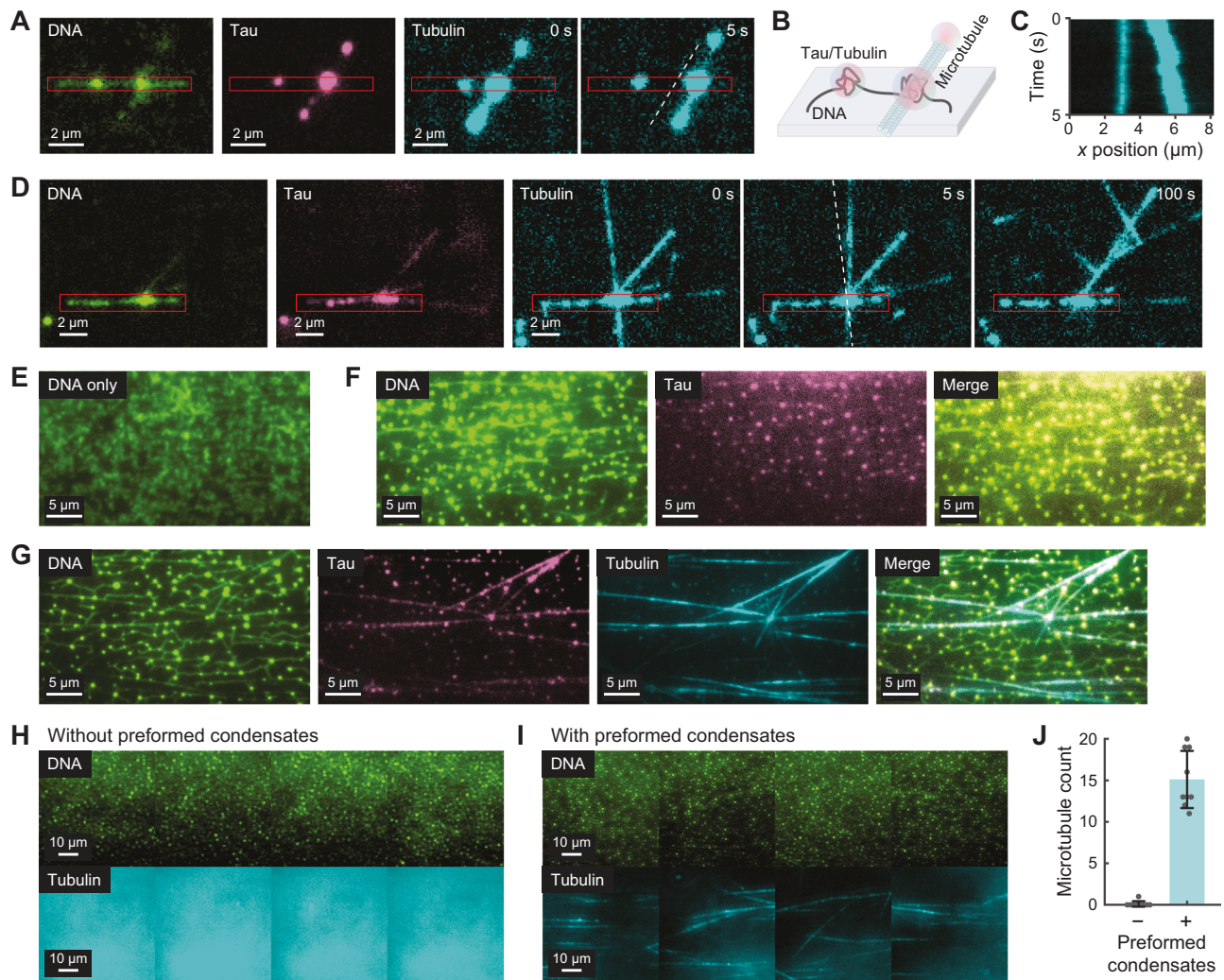


**Fig. 4 | Microtubules interfacing with tau-DNA co-condensates.** **A** Snapshots showing the dynamic gliding of microtubules (cyan, labeled with HiLyte 488,) along DNA (green, stained with SYTOX Orange), driven by the mobility of tau condensates (magenta, labeled with Cy5) on DNA. Microtubules were formed by incubating with 5  $\mu$ M tubulin. **B** Schematic illustration of the DNA-tau-microtubule tripartite assembly. **C** Representative kymograph displaying the mobility of the gliding microtubule on DNA shown in (A). **D** Time-lapse images capturing the pivoting motion of the microtubule, anchored by tau-DNA co-condensates. In (A) and (B), red boxes mark the location of the DNA strands, and white dashed lines show the position of the microtubules in the preceding image. **E-G** TIRF images of high-density surface-tethered  $\lambda$ -DNA (green, stained with SYTOX Orange) before tau addition (E), after adding 5  $\mu$ M tau (magenta, Cy5-labeled) with 5% PEG (F), and after adding a mixture of tau and tubulin (cyan, HiLyte 488-labeled) with 5% PEG (G). Microtubules were pulled to the surface by tau-DNA co-condensates. **H, I** Large-area views of microtubule pull-down on DNA surfaces with and without preformed tau-DNA co-condensates. In (H), microtubules did not attach to the DNA surface without tau pre-incubation to form condensates; only background fluorescence from out-of-focus tubulins was visible. **J** Quantification of surface-bound microtubules with and without preformed tau-DNA co-condensates ( $n = 9$  images; mean  $\pm$  s.d.).

tubulin also localized within the tau condensates (Fig. 4A), indicating that these spots might serve as seeds for nucleating new microtubules. The microtubules engaged with the DNA strands either along their sides or via their ends, analogous to the lateral and end-on attachments posited for mitotic spindle coupling to chromosomes during mitosis<sup>41</sup>.

Intriguingly, microtubules attached to both singly and doubly tethered DNA strands exhibited dynamic behaviors, including diffusive movements along DNA due to mobile condensates (Fig. 4A-C, Supplementary Movie 6) and pivoting around anchoring tau condensates (Fig. 4D, Supplementary Movie 7). This was particularly evident in the occasional diffusive translation of entire microtubule filaments along double-tethered DNA substrates. With a slight increase in DNA surface density, more microtubules were captured, and tau clusters on different DNA strands cooperatively bridged and bundled nearby microtubules, forming a tripartite network of DNA, tau, and microtubules (Supplementary Movie 8). These observations suggest that tau

condensates may facilitate the repositioning and stabilization of microtubules relative to DNA, in processes such as mitotic spindle attachment to chromosomes.

To directly demonstrate the role of tau condensates in microtubule capture, we designed a microtubule capture assay in a more complex environment with higher concentrations of tau and DNA. In this assay, we densely packed the surface with DNA (Fig. 4E, Supplementary Movie 9), allowing multiple strands to collaboratively induce tau condensation. We increased the tau concentration to 5  $\mu$ M and added 5% PEG to simulate molecular crowding. The formation of tau-DNA co-condensates appeared as discrete bright nodes interconnected by surface-tethered DNA, which manifested as thin, dimmer lines forming a reticular network (Fig. 4F, Supplementary Movie 9). The tau-DNA co-condensates appeared as distinct bright foci, while the surface-tethered DNA formed an intricate mesh connecting these nodes. This reticular structure suggests a complex and organized

arrangement of tau–DNA interactions, highlighting tau’s ability to induce localized DNA condensates while maintaining a networked distribution across the nucleic acid surface, similar to the behavior of various DNA-compacting proteins. Under this condition, the overall structure became more stabilized, and the mobility of tau locations was significantly reduced (Supplementary Movie 9).

Under these conditions, tau–DNA clusters at distant sites were able to cooperatively recruit longer microtubules (Fig. 4G, Supplementary Movie 9), effectively bridging the gap in length scale. Since the DNA molecules were arranged on a 2D plane, the captured microtubules conformed to the substrate surface. Most importantly, when tau condensates were not preformed before the introduction of tubulin, only a few surface-bound microtubules were observed (Fig. 4H vs. 4I), despite the presence of numerous microtubules away from the DNA surface (Supplementary Movie 10), contributing to background fluorescence. By quantifying the number of microtubules attached to the DNA surface, we confirmed that the presence of preformed tau–DNA co-condensates is indeed critical for capturing microtubules from the solution (Fig. 4J). We propose that this conformational attachment of microtubules to a densely packed DNA surface via tau–DNA co-condensates may represent a mechanism for docking nascent microtubules to complex DNA structures, such as mitotic chromosomes.

### Phosphorylated tau retains DNA binding and enables microtubule capture with wild-type tau

Microtubule dynamics are tightly regulated by tau and its phosphorylation state, particularly during mitosis when increased phosphorylation correlates with enhanced microtubule turnover. Although tau contains up to 85 potential phosphorylation sites, only a small subset is modified under physiological conditions<sup>42</sup>. In healthy brains, tau carries an average of 2–3 phosphate groups, while aberrant forms found in Alzheimer’s disease exhibit 3–4 times higher levels, contributing to tau aggregation<sup>43</sup>. To determine how phosphorylation alters tau’s DNA condensation and microtubule-recruiting capacity, we phosphorylated human 2N4R tau *in vitro* with cAMP-dependent protein kinase (PKA), which primes tau for subsequent modification by GSK-3 $\beta$ <sup>44</sup>. Efficient phosphorylation was confirmed by the characteristic upward shift on SDS–PAGE (Supplementary Fig. 1). Site-specific verification by LC–MS/MS confirmed strong phosphorylation at known PKA target sites (Supplementary Fig. 1), including S214, S324, S352, S356, S409, and S416, consistent with previous reports<sup>25,45</sup>. These modifications collectively yield an overall phosphorylation occupancy of ~4 sites per tau molecule.

PKA-phosphorylated tau (pTau) was then introduced either onto  $\lambda$ -DNA tethers to assess condensation or into the tubulin mix during nascent microtubule polymerization (Fig. 5A). Although pTau retained DNA-binding and condensate-forming activity, both activities were modestly reduced compared to wild-type (WT) tau (Fig. 5B, C). Next, in microtubule capture assays, pTau–DNA condensates recruited fewer microtubules when exposed to filaments formed with WT tau and tubulin (Fig. 5D, E). Unexpectedly, when microtubules were polymerized with pTau, the shorter, less stable filaments still attached efficiently to WT tau–DNA condensates, as indicated by intense fluorescence from bound segments (Fig. 5D, F). This suggests that dynamic pTau-associated microtubule fragments can engage tau–DNA condensates in the presence of WT tau. By contrast, assays using pTau for both DNA condensation and microtubule assembly produced only tubulin aggregates on the DNA surface, without filamentous structures, demonstrating that pTau alone lacks robust microtubule-interfacing ability. Together, these findings indicate that although phosphorylation diminishes tau’s affinity for DNA and microtubules, pTau-associated microtubule fragments during mitotic progression can still interact with tau–DNA co-condensates when WT tau is available.

### Nucleosome arrays support tau binding and microtubule recruitment

To place our *in vitro* observations in a more physiologically relevant context, we replaced  $\lambda$ -DNA with a 2.3-kb dsDNA bearing 12 Widom-601 sites (Fig. 5G), reconstituted nucleosomes on this template, and repeated the tau-binding and microtubule-capture assays. A set of biochemical and biophysical assays indicated densely loaded, stable nucleosome arrays (see Supplementary Note 2, “Verification of Nucleosome Assembly on 601 DNA”, and Supplementary Figs. 10–11). For a controlled comparison to naked DNA, we also prepared naked 601 DNA (no nucleosome reconstitution) at similar surface density for imaging (Fig. 5H, I). Because the 601 construct is much shorter than  $\lambda$ -DNA (2.3 kb vs. 48.5 kb), individual DNA strands were not resolvable by TIRF. Upon adding 5  $\mu$ M tau, discrete tau clusters formed and colocalized with H2A-labeled nucleosomes (Fig. 5J). Although overall tau binding was lower than on  $\lambda$ -DNA, likely reflecting the shorter template length, colocalization analysis showed a high correlation between nucleosome and tau signals for both nucleosomal and naked 601 DNA at near-comparable levels (Fig. 5K).

Finally, introducing a tau–tubulin mixture containing nascent microtubules yielded robust microtubule capture on surfaces bearing nucleosome-pinned tau clusters (Fig. 5L), comparable to  $\lambda$ -DNA-induced condensates (Fig. 4J). Microtubule counts were indistinguishable between naked DNA and nucleosome arrays (Fig. 5M), despite the reduced amount of free DNA segments in the latter. Together, these data suggest that nucleosomal DNA remains competent to recruit tau and interface with microtubules to a similar extent as its naked-DNA counterpart, consistent with recent bulk measurements of tau association with nucleosome arrays and linker DNA<sup>25</sup>.

### Tau clusters localize on centromeres during prometaphase of mitosis

The tripartite assembly of DNA, tau, and microtubules we observed *in vitro* led us to hypothesize a role for tau in the division of tau-expressing cells, especially in how nascent mitotic spindles capture chromosomes. To test this in a neuronal setting, we conducted immunofluorescence imaging of SH-SY5Y cells, a neuroblastoma line that endogenously expresses tau. Immunostaining of thymidine-synchronized, dividing cells (identified by condensed chromosomes) revealed a consistent level of endogenous tau forming small puncta with distinct distributions across mitotic stages (Supplementary Fig. 12). We focused on cells in prometaphase, just before chromosome congression, which typically displayed the characteristic rosette structure formed by mitotic chromosomes surrounding the nascent spindle (Fig. 6A). These images revealed strong colocalization between tau and tubulin, indicating that tau remains closely associated with microtubules during prometaphase. Notably, tau formed distinct clusters on mitotic chromosomes, most of which colocalized with centromeres labeled by CREST anti-centromere antibody (Fig. 6A, magnified views in the bottom panels). To quantitatively assess the colocalization between tau and centromeres, we pooled images of 181 centromeres from 11 prometaphase cells and averaged them after precise alignment (Fig. 6B). Intensity profiles of centromeres and tau fluorescence in these averaged images indeed showed a clear overlap. Pearson correlation coefficients calculated for each SH-SY5Y cell image confirmed strong colocalization of tau with both tubulin and centromeres (Fig. 6C, D). Interestingly, prophase SH-SY5Y cells also revealed clear association of nuclear tau with centromeres (Supplementary Fig. 12), consistent with its known pericentromeric localization<sup>39,46</sup>.

To extend these findings beyond a neuronal context, we next turned to HEK-293 cells, which have low endogenous tau. We transiently expressed mCherry-tagged 2N4R tau and synchronized the cells in the same way. Confocal imaging of mCherry fluorescence for tau, alongside immunostaining for tubulin and centromeres (CREST

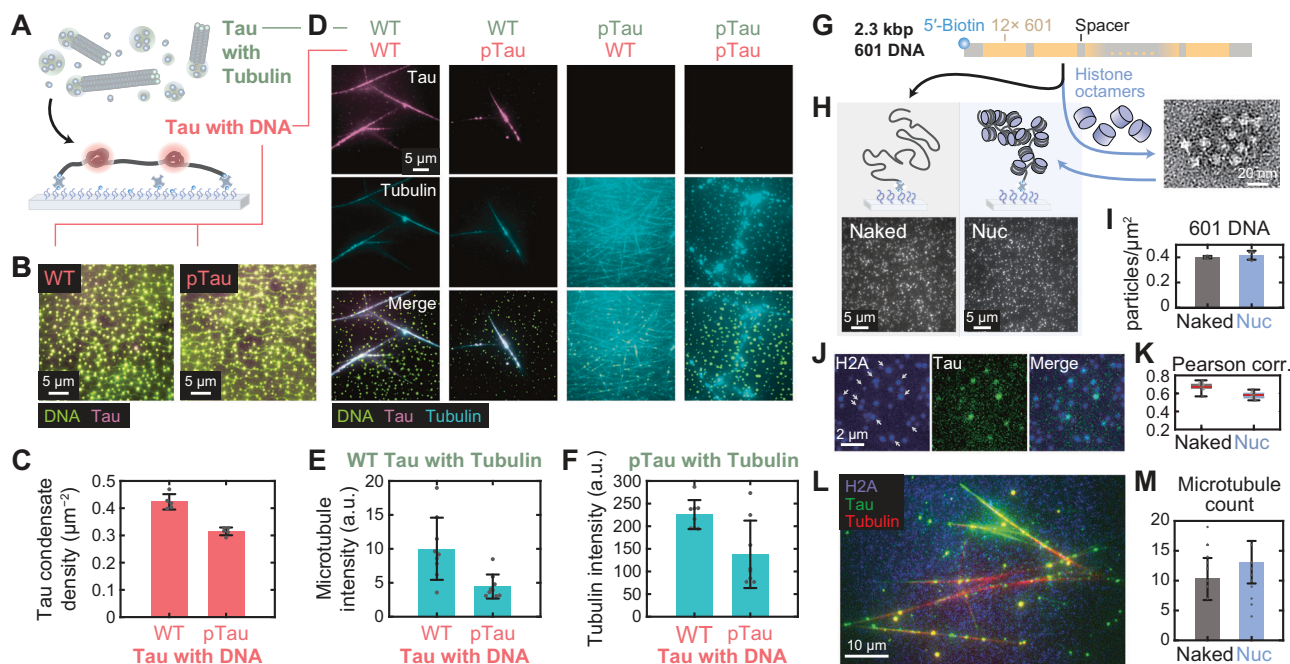


**Fig. 5 | Microtubule capture by tau–DNA co-condensates with nucleosomes and phosphorylated tau.** **A** Schematic of the microtubule capture assay using two tau conditions: pre-formed tau–DNA condensates or polymerizing microtubules. **B** Comparison of tau–DNA co-condensate formation with wild-type (WT) and protein kinase A (PKA)-phosphorylated tau (pTau). **C** Quantification of tau condensate density for WT and pTau on DNA substrates ( $n = 5$  images; mean  $\pm$  s.d.). **D** TIRF images of tau (magenta) and microtubules (cyan) observed with different combinations of WT and pTau. DNA (green) is shown in the merged images. **E** Fluorescence intensity (in arbitrary units) of WT tau-polymerized microtubules recruited by WT versus pTau condensates ( $n = 9$  images; mean  $\pm$  s.d.). **F** Fluorescence intensity of tubulin captured by tau–DNA condensates ( $n = 8$  images; mean  $\pm$  s.d.). **G** Schematic of the 2.3-kb DNA construct bearing 12 repeats of the Widom-601 nucleosome positioning sequence. The construct was used either as

naked 12 $\times$ 601 DNA or assembled into nucleosomes (Nuc) with purified histone octamers. Negative-stain TEM of the assembled sample (*inset*) showed beads-on-a-string arrays with  $\sim 12$  nucleosomes per DNA and uniform spacing (for more images, see Supplementary Fig. 11). **H** TIRF fields of view for naked and nucleosomal conditions at matched surface density. **I** 601 DNA particle densities for the conditions shown in (**H**) ( $n = 5$  images; mean  $\pm$  s.d.). **J** Fluorescence images of nucleosomes (Alexa 488–H2A) and Cy3-labeled tau; arrows mark H2A puncta that colocalize with tau. **K** Pearson correlation between nucleosome and tau signals for the images in (**J**) ( $n = 9$  images). Box plot shows median (red line), interquartile range, and whiskers to the minimum/maximum. **L** Fluorescence images of nucleosomes (Alexa 488–H2A), tau (Cy3), and microtubules (HiLyte 647–labeled tubulin). **M** Microtubule counts per field for the conditions shown in (**L**) ( $n = 11$  images; mean  $\pm$  s.d.).

antibody), again showed tau clusters on the prometaphase rosette of mitotic chromosomes and tight colocalization with spindle microtubules (Fig. 6E). Analysis of 460 centromeres from 18 prometaphase HEK-293 cells verified overlap between tau and centromere signals (Fig. 6F), mirroring our SH-SY5Y results and supporting tau's role in chromosome–spindle attachment. Again, Pearson correlation across these cell images quantified strong colocalization of tau with both tubulin and centromeres (Fig. 6C, D).

To assess whether tau directly associates with mitotic chromosomes at higher resolution, we prepared chromosome spreads from these HEK-293 cells expressing mCherry–Tau (Fig. 6G). In these preparations, small punctate tau clusters decorated the surface of condensed chromosomes, demonstrating that tau retains its DNA-binding activity within a chromatin context. We did not observe centromere-specific enrichment in this case, likely because the more transient or weak interactions that mediate centromere recruitment are disrupted during the spreading.

While native HEK-293 cells showed no detectable tau, transient expression of 2N4R mCherry–Tau produced tau levels far exceeding those in SH-SY5Y (Fig. 6H). To probe whether tau expression alters cell-cycle behavior, we performed RNA-seq on these HEK-293 cells. Tau expression caused modest transcriptomic changes (Fig. 6I), including upregulation of stress-response genes CHAC1, ATF3, HMOX1, and DDIT3. We also observed downregulation of CENPE, involved in chromosome movement, and BRCA2, a key DNA-repair and cell-cycle regulator (Fig. 6J). These shifts mainly affected cell-division,

microtubule-organization and DNA-repair pathways, consistent with a mitotic role for tau. Despite these transcriptomic shifts, overall proliferation was largely unchanged, likely because other mitotic factors compensate for tau's function in its absence.

Collectively, these findings highlight the consistent involvement of tau in interfacing microtubules with centromeres during mitosis in tau-expressing cells, whether tau is present endogenously or introduced exogenously.

### Phosphomimetic tau mutants condense DNA but differ in microtubule-interfacing potential

Phosphorylation of tau at multiple sites is tightly regulated by various kinases and phosphatases, influencing its affinity for microtubules<sup>47</sup>. To investigate how phosphorylation-like changes affect tau–DNA interactions and their role in recruiting microtubules, we generated two additional recombinant tau proteins with phosphomimetic mutations: T231D/S235D (a double mutant) and S262D. Given the critical association of these sites with microtubule binding and Alzheimer's disease<sup>48–51</sup>, these mutants are often used to model pathological modifications seen in tauopathies<sup>52–55</sup>.

We first confirmed through single-molecule experiments that both T231D/S235D and S262D tau proteins successfully undergo co-condensation with DNA, similar to wild-type tau (Fig. 7A). Next, we examined whether these mutants could still support the assembly of the DNA–tau–microtubule network. When mixed with tubulin in the presence of GTP, the phosphomimetic mutants were able to nucleate

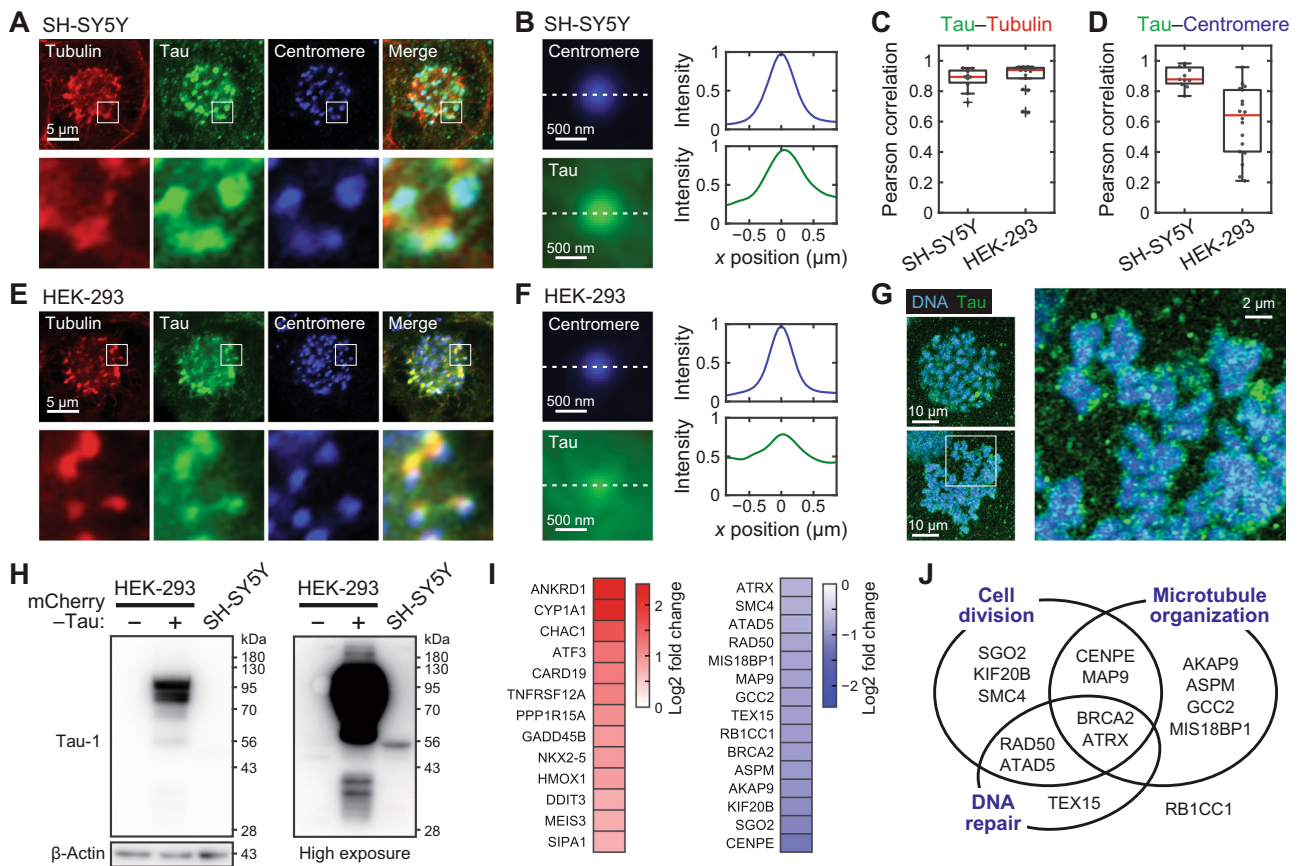


**Fig. 6 | Localization of tau on centromeres during cell division.**

**A** Immunofluorescence images of prometaphase SH-SY5Y cells endogenously expressing tau showing the distribution of tubulin, tau, and centromeres. Centromeres were specifically labeled using an anti-centromere (CREST) antibody. **B** Intensity profiles of centromere (top blue) and tau (bottom green) measured across aligned centromere regions. Centromere images were collected from multiple regions ( $n = 181$  centromeres from 11 cells), aligned, and analyzed for the presence of tau signal. **C, D** Pearson correlation coefficients for tau colocalization with tubulin and centromeres, calculated from the cell images used in **(B)** and **(F)**. Box plots show median (red line), interquartile range, and whiskers to the minimum/maximum; each point represents one cell. **E, F** Same as **(A)** and **(B)**, but in HEK-293 cells expressing mCherry–Tau ( $n = 460$  centromeres from 18 cells for **(F)**).

**G** Confocal images of chromosome spreads from mitotic HEK-293 cells expressing mCherry–Tau (green) and stained with Hoechst 33258 (blue); the right-hand panel shows a magnified view of the white-boxed region. **H** Western blot of tau in native HEK293 cells, HEK293 cells transfected with mCherry–tau, and native SH-SY5Y cells. The left panel shows a standard exposure, and the right panel shows a high exposure to reveal the faint SH-SY5Y band. A representative blot from  $n = 3$  biologically independent experiments is shown. Both panels were generated from a parallel membrane loaded with identical samples and processed under the same experimental conditions. **I** List of top up- (left) and down-regulated (right) genes in HEK-293 cells transiently expressing mCherry–Tau ( $\log_2$  fold change  $> 0.7$  or  $< -0.7$ ;  $p < 0.05$ ). **J** Venn diagram for the down-regulated genes shown in **(I)**, involved in cell division, microtubule organization, and DNA repair pathways.

microtubule growth, though to a much lesser extent than wild-type tau (Fig. 7B). Specifically, the microtubules formed in the presence of these mutants were shorter, less bundled (as indicated by a dimmer appearance), and depolymerized more rapidly compared to those formed with wild-type tau (Supplementary Fig. 9). Nonetheless, in this buffer condition, microtubule growth was entirely absent without tau, indicating that the tau mutants still retain some microtubule-binding activity. As a result, wild-type tau outperformed the phosphomimetic mutants in promoting microtubule growth, as reflected by the higher microtubule count (Fig. 7C). These findings are consistent with previous observations that phosphorylated tau has impaired microtubule binding, leading to a reduced stabilizing effect.

To compare the capacity of different tau mutants to couple microtubules to DNA, we performed a microtubule capture assay using tau–DNA co-condensates, as described above for wild-type tau (Fig. 4G). The images of microtubules on the DNA surface were largely indistinguishable between wild-type and the T231D/S235D mutant. However, in the case of the S262D mutant, almost no microtubules were observed; instead, clustered aggregates of tubulin formed (Fig. 7D). Quantification of the microtubule count revealed that, despite its impaired ability to promote microtubule formation in

solution (Fig. 7B, C), the T231D/S235D tau mutant captured and interfaced with microtubules on the DNA surface at a level comparable to wild-type tau (Fig. 7D, E). This suggests that the T231D/S235D mutant retains a particularly strong capacity for mediating interactions between DNA and microtubules, even though it exhibits reduced microtubule nucleation and bundling overall. In contrast, the S262D mutant showed a marked decrease in microtubule capture on the DNA surface, presumably due to its impaired microtubule binding and stabilization<sup>49</sup>. Overall, these results suggest that tau’s ability to interface between DNA and microtubules may be regulated by site-specific phosphorylation.

### Phosphomimetic tau localizes to centromeres but impairs chromosome alignment

To test whether the *in vitro* differences in DNA–microtubule interfacing by phosphomimetic tau mutants manifest in cells, we performed immunofluorescence on mitotic HEK-293 cells transiently expressing mCherry-tagged T231D/S235D or S262D tau, using the same approach as for wild-type tau (Fig. 6). Although both mutants largely retained microtubule binding during mitosis (Fig. 7F), Pearson correlation analysis revealed their reduced association with spindle microtubules

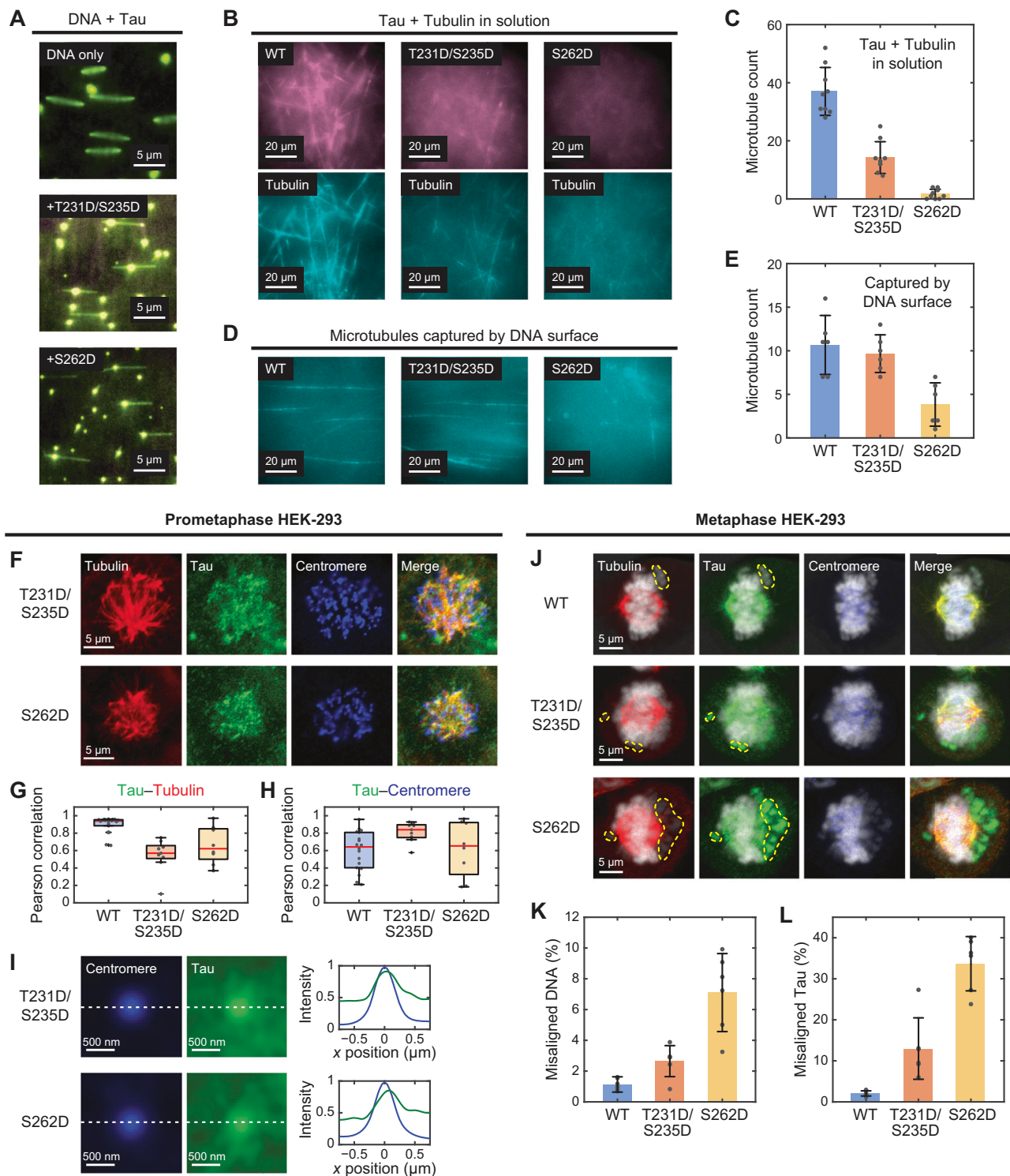


**Fig. 7 | Phosphomimetic tau mutants in DNA-tau-microtubule assembly, centromere localization, and chromosome congression.** **A** TIRF images (time-averaged projection over 5 s) of DNA alone (*top*) and DNA incubated with the indicated tau mutants (T231D/S235D and S262D). **B** Microtubule formation in solution in the presence of wild-type (WT) or the indicated phosphomimetic tau. **C** Quantification of microtubule counts in the tau-tubulin mixture ( $n = 9$  images; mean  $\pm$  s.d.), as shown in (**B**). **D** Large-area views of microtubule capture on the DNA surfaces with tau condensates formed by the indicated species. **E** Quantification of microtubule counts on the surface captured by DNA ( $n = 6$  images; mean  $\pm$  s.d.), as shown in (**D**). **F** Immunofluorescence images of prometaphase HEK-293 cells transiently expressing phosphomimetic (T231D/S235D and S262D) mCherry-Tau, showing the distribution of tubulin, tau, and centromeres. **G**, **H** Pearson correlation coefficients for tau colocalization with tubulin and centromeres ( $n = 9$  cells for

T231D/S235D,  $n = 8$  cells for S262D). Box plots show median (*red line*), interquartile range, and whiskers to the minimum/maximum; each point represents one cell. For comparison, the wild-type tau data from Fig. 6C, D are reproduced here. **I** Intensity profiles of centromere (*blue*) and tau (*green*) measured across aligned centromere regions, obtained from the cell images used in (**G**) and (**H**) ( $n = 429$  centromeres for T231D/S235D,  $n = 288$  centromeres for S262D). **J** Immunofluorescence of metaphase HEK-293 cells expressing WT or phosphomimetic mCherry-Tau. DNA image (Hoechst 33258-stained) is overlaid in gray for reference. Misaligned DNA foci away from the metaphase plate is outlined in yellow. In (**F**), (**I**), and (**J**), centromeres were specifically labeled using an anti-centromere (CREST) antibody. **K**, **L** Quantification of misaligned DNA (Hoechst 33258) and tau (mCherry) intensities, normalized to each cell's total signal ( $n = 6$  images each; mean  $\pm$  s.d.).

(Fig. 7G), consistent with the impaired microtubule-stabilizing activity (Fig. 7B). Nevertheless, both mutants exhibited robust centromeric localization comparable to wild-type tau (Fig. 7H), reflecting their retained DNA-binding activity (Fig. 7A). Analysis of averaged centromere images further confirmed overlapping tau signal (Fig. 7I).

Surprisingly, in metaphase cells after chromosomes have aligned at the metaphase plate, both phosphomimetic mutants showed prominent tau-rich chromosomal regions that failed to align (Fig. 7J). These tau–DNA clusters did not colocalize with the central tubulin signal, indicating a lack of spindle attachment, and were most frequent in S262D-expressing cells, implicating aberrant tau–DNA binding in defective microtubule capture. Quantitative analysis of DNA and tau amount (measured by Hoechst 33258 and mCherry fluorescence, respectively) confirmed these findings. In S262D cells, misaligned DNA foci comprised about 10% of total chromosomal DNA, significantly more than in wild-type or T231D/S235D cells (Fig. 7K; see Supplementary Fig. 13 and Supplementary Methods for analysis). Tau fluorescence at these foci accounted for nearly 30% of total cellular tau in S262D cells—over a five-fold increase versus wild type (Fig. 7L). These data demonstrate that phosphomimetic tau mutants not only lose their ability to engage spindle microtubules but also aberrantly accumulate on misaligned chromatin, thus compromising proper chromosome segregation.

## Discussion

Despite extensive research, many aspects of tau biology remain unclear, including its functions beyond microtubule stabilization and the mechanisms underlying tauopathies. Our results demonstrate through single-molecule experiments that tau binds strongly to naked DNA and forms dynamic condensates, thereby inducing local compaction of DNA (Figs. 1 and 2). The microtubule-binding region (MTBR) of tau is enriched in basic residues that likely confer an overall affinity for polyanions such as DNA, consistent with the salt dependence of tau–DNA binding (Fig. 2). A previous NMR study mapped the DNA-binding region of tau to the proline-rich domain and R2 region<sup>24</sup>, and a recent biophysical study showed a strong salt dependence of tau–DNA and tau–chromatin associations<sup>25</sup>, consistent with an electrostatic picture. However, the full energetics of tau–DNA co-condensation are likely shaped by a combination of electrostatic and hydrophobic interactions<sup>6,16,22,56</sup>, similar to the well-known LLPS behavior of tau alone or with RNA and RNA-binding proteins<sup>4,13–15,17</sup>. Interestingly, despite the largely nonspecific nature of tau–DNA interactions, we observed a slight preference for AT-rich regions in condensate positioning (Supplementary Fig. 6), in agreement with gel assays and tau's association with  $\alpha$ -satellite DNA sequences<sup>39</sup>. Because tau-induced DNA compaction involves bending of DNA segments (see below for mechanical discussion), the observed sequence dependence would combinedly reflect both biophysical dynamics and biochemical affinity. Importantly, this *in vitro* result does not account for the influence of additional cellular components.

The liquid-like properties of tau clusters on DNA, including their mobility (Fig. 2) and content exchange (Supplementary Fig. 5), are reminiscent of phase-separated condensates in free solution, as systematically investigated by Abasi *et al.*<sup>25</sup>. We further showed that tau–DNA co-condensation occurs below the critical saturation concentration ( $c_{\text{sat}}$ ) (50–100  $\mu\text{M}$  for tau alone or  $>1\ \mu\text{M}$  under crowding conditions<sup>5,6,30</sup>), suggesting that DNA strands can enrich the local concentration of tau. DNA binding effectively reduces the dimensionality of tau clustering (from 3D to quasi-ID), potentiating condensation similarly to LLPS on 2D lipid membranes<sup>57</sup>. With total tau levels in the brain ranging from 1 to 7  $\mu\text{M}$ <sup>58–60</sup> and a sub-micromolar nuclear fraction<sup>61</sup>, the concentrations we tested (50 nM to 5  $\mu\text{M}$ ) span early tau–DNA binding events at the low to physiological and pathologically elevated tau levels at the high end.

Additionally, our mechanical analysis using magnetic tweezers (Fig. 3) showed that tau binding to DNA is strongly cooperative, thus driving condensation below  $c_{\text{sat}}$ . Given the contour length of dsDNA ( $\sim 0.34\ \text{nm bp}^{-1}$ ), the 50–70-nm increments observed during the stretching of tau–DNA co-condensates (Fig. 3F) correspond to 150–200 base pairs. This is intriguingly close to the persistence length of dsDNA ( $\sim 150\ \text{bp}$ ), suggesting that tau condensates compact DNA into domains of this characteristic size, set by the helix's bendability. Indeed, our simulations reproduce these steps of similar sizes (Fig. 3I), each reflecting the force-induced rupture of an individual tau–DNA cluster. The minor groove binding of tau to the DNA backbone<sup>21</sup> may sculpt this specific compaction, helping tau overcome the intrinsic stiffness of dsDNA and promoting the formation of more organized structures. Additionally, dynamic reorganization of existing tau clusters before reaching equilibrium may contribute to the stepwise changes in DNA extension. The all-or-none behavior during the condensation phase also supports the cooperative nature of tau condensation on DNA, rapidly drawing nearby DNA segments into maturing tau condensates. Further structural studies on tau–DNA complexes using cryo-electron microscopy or X-ray crystallography will be in order. Similar protein–DNA co-condensation behaviors are being discovered in other DNA-binding proteins<sup>31,34–37</sup>, which can generate forces on DNA<sup>33</sup> as demonstrated in our tweezer experiments. Capillary forces and dynamic instability are expected to regulate the formation and coalescence of these condensates<sup>62,63</sup>, influencing their size, shape, and interactions with surrounding structures, including microtubules.

We demonstrate *in vitro* that tau–DNA co-condensates can capture and organize microtubules, acting as dynamic hubs (Fig. 4). It is surprising that microtubules did not attach to DNA without preformed tau condensates (Fig. 4H–J), even when the microtubule solution contained the same concentrations of tau and PEG used during preincubation. This indicates that tau condensates on DNA are fundamentally distinct from those formed with tubulin, which may be explained by conformational changes in tau upon DNA binding that enhance microtubule interaction. Indeed, the DNA-binding region of tau is proposed to partially overlap with MTBR<sup>24</sup>, supporting the conformational priming model. Beyond this monomer-level mechanism, we favor a larger-scale, multivalent mode of affinity arising from clustered tau molecules, potentially involving a composite tau–DNA interface. These two mechanisms (conformational priming and condensate-mediated multivalent recruitment) are not mutually exclusive and likely act together to promote robust microtubule binding.

The unexpected enrichment of tau at centromeres during prometaphase in both SH-SY5Y (endogenous tau) and HEK-293 (exogenous tau) cells (Fig. 6) occurs despite tau's largely nonspecific affinity for DNA. This preference aligns with tau's subnuclear localization to HP1 $\alpha$ -marked pericentromeric heterochromatin<sup>39,46</sup> and its chromatin-related functions<sup>64,65</sup>. Although the tripartite assembly of tau–DNA–microtubule itself does not necessarily invoke the nuclear function of tau<sup>28</sup>, we speculate that centromeric tau condensates that assemble in the nucleus during prophase (Supplementary Fig. 12) may behave analogously to our *in vitro* preformed condensates, guide the migration of tau on other chromosomal sites toward the centromeres, and then merge with cytosolic tau clusters on microtubules after nuclear envelope breakdown. Future experiments should employ prolonged live-cell imaging to validate this idea.

*In vitro* formation of tau clusters on nucleosome arrays, which retain the ability to mediate microtubule assembly (Fig. 5), may partially explain how tau condensates form on nucleosome-rich centromeres in dividing cells. Across assays, nucleosomal 601 DNA bound tau and supported microtubule binding at levels comparable to its naked-DNA counterpart. Since fully loaded 601 DNA leaves only short

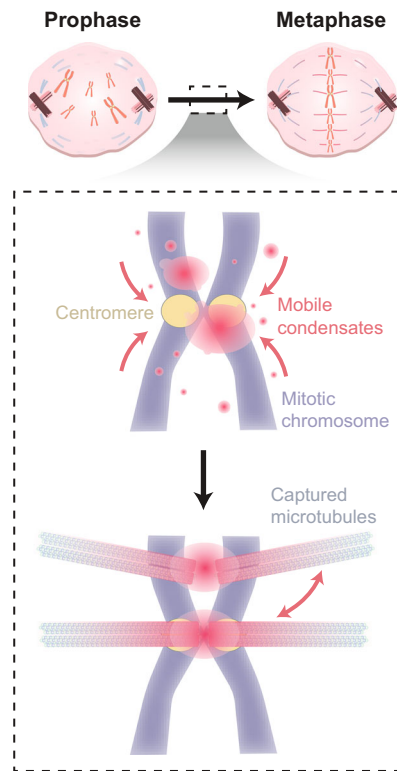


**Fig. 8 | Tau condensation on DNA and localization on centromeres: A potential link to cell division.** A model for the mitotic function of tau–DNA co-condensation and its centromere localization during mitosis. In prometaphase, tau forms mobile condensates on chromosomes, aiding in the capture and dynamic rearrangement of nascent microtubules. As these condensates merge and migrate toward centromeres, stable chromosome–spindle connections are established via kinetochores.

stretches of free DNA, this suggests that nucleosome-wrapped DNA segments still provide effective binding sites for tau. Although our TIRF imaging could not resolve whether tau predominantly associates with free linker DNA or with nucleosome cores, this interpretation is consistent with a recent bulk study reporting strong complexation of tau with nucleosome arrays and comparable nanomolar affinities for both nucleosomal and naked DNA<sup>25</sup>. It will be informative to track tau's motions on longer DNA substrates (e.g.,  $\lambda$ -DNA) to test whether tau drives nucleosome rearrangements with potential epigenetic consequences. Given tau's centromeric enrichment, it will be important to examine tau–nucleosome interactions with CENP-A nucleosomes, whose more flexible DNA ends may afford greater access to free DNA segments<sup>66</sup>.

The multivalent nature of tau may be fine-tuned by post-translational modifications such as phosphorylation and acetylation. These modifications, which adjust tau's charge, may act as switches controlling its partitioning between microtubules and DNA<sup>67</sup>. Notably, tau phosphorylation is an important mechanism for regulating microtubule stability and is controlled in a cell cycle-dependent manner<sup>68–71</sup>. Based on the differential effects of enzymatic phosphorylation and phosphomimetic variants (Figs. 5 and 7), we propose that multisite phosphorylation fine-tunes tau's affinity for DNA and microtubules and regulates their dynamic interplay. Because our microtubule capture assay was specifically configured to distinguish DNA-preformed from tubulin-associated condensates, the distinct activities of unphosphorylated versus phosphorylated tau in these two contexts (Fig. 5A–F) provide a support for our two-stage model of

nuclear-origin and spindle-associated condensates, in line with the high phosphorylation state of cytosolic tau during mitosis.

Tau's ability to bridge microtubules to DNA, together with its strategic localization between mitotic spindles and centromeric DNA in dividing cells, suggests a role for tau in attaching nascent mitotic spindles to chromosomes during neuronal cell division, facilitating the random “search and capture” process<sup>29</sup>. We propose that (Fig. 8): (i) in prometaphase, tau condenses on DNA substrates, including chromosomes; (ii) the dynamic condensates locally remodel DNA structures and facilitate the docking of nascent spindle microtubules, predominantly via lateral-surface interactions<sup>72</sup>; and (iii) as the condensates mature toward centromeres, these initial attachments are progressively replaced by stable end-on kinetochore contacts required for metaphase congression<sup>73</sup>. The idea of tau's involvement in chromosome-spindle linkage was first considered in the 1980s<sup>74</sup> but has not been thoroughly explored, with experimental evidence remaining limited. However, more evidence is required for a stringent test of this hypothesis, including the effects of tau depletion or mutations that specifically interfere with tau–DNA interactions. Note that this model is also compatible with other mechanisms that facilitate chromosome capture and biorientation through alternative pathways<sup>41,75–77</sup>.

The failure of some chromosomes to align at the metaphase plate in cells expressing Alzheimer's-associated phosphomimetic tau mutants is informative in this regard (Fig. 7J–L). It suggests that altered phosphorylation could disrupt tau's dynamic partitioning between DNA and microtubules, remain abnormally coated on chromatin, and escape timely spindle capture, potentially contributing to chromosome missegregation and aneuploidy. These cell-based findings not only validate the biophysical function of tau observed *in vitro* but also reflects the loss-of-function effect seen in microtubule capture assays. This bidirectional correspondence strongly reinforces the idea that site-specific phosphorylation of tau disrupts its mitotic function. The transcriptomic shift observed in HEK-293 cells upon tau expression (Fig. 6I, J) likely reflects a mild cellular response to excess tau<sup>78–80</sup>, consistent with its expected influence on microtubule dynamics, but may also point to additional roles in DNA protection<sup>25,26,81,82</sup> or broader signaling pathways<sup>83</sup>. However, these shifts did not significantly disrupt cell division, allowing us to examine tau during mitosis without inducing excessive cellular stress.

Because tau is not constitutively expressed in most cell types, its mitotic function via tau–DNA co-condensation is likely restricted to contexts with elevated tau levels. In tau-deficient cells, other MAP family members may compensate for its absence. It will therefore be of interest to determine whether these proteins can similarly co-condense with DNA, localize to centromeres, and mediate microtubule capture during mitosis. Given the link between aberrant cell cycle activation in postmitotic neurons and neurodegeneration<sup>84–86</sup>, as well as the reduction of adult hippocampal neurogenesis in cognitive decline<sup>87,88</sup>, it is possible that the defective mitotic function of tau in neurons could have broader implications for neurodevelopment and neurodegeneration. It is tempting to postulate that hyperphosphorylation of tau, long associated with tauopathies<sup>47,89,90</sup>, may also contribute to chromosome missegregation through disrupted tau–DNA co-condensates. We further contemplate the potential connection between our findings and tau expression in cancer<sup>91–94</sup>, where disrupted mitotic signaling may provoke dysregulated tau activity during cell division, leading to chromosome instability and ultimately aneuploidy, a hallmark of cancer.

Future studies on tau diversity, including developmental isoforms, pathogenic mutations, and phosphorylation status, each of which can alter its LLPS behavior and/or microtubule dynamics<sup>5,42,95–97</sup>, will explore how these changes impact tau–DNA co-condensation and the subsequent DNA–tau–microtubule assembly.

## Methods

### Protein purification and labeling

The cDNA encoding the 6×His-tagged 2N4R isoform of human tau was cloned into the pRK172 vector (a gift from the Feinstein lab, UCSB) and expressed in LEMO21 cells (NEB #C2528J). For preparing phosphomimetic tau mutants, site-directed mutagenesis was performed on the wild-type plasmid via overlap-extension PCR (primer sequences provided in Supplementary Data 1), and the resulting products were assembled into full-length plasmids using Gibson assembly (NEB, #E2611S). For bacterial expression, cells were cultured in TB media at 37 °C until the OD<sub>600</sub> reached 0.6, followed by treatment with 10 mM betaine and 500 mM NaCl. After a 30-min incubation at 30 °C, 0.4 mM IPTG was added, and the culture continued for an additional 3–4 h. The cells were homogenized and lysed in lysis buffer (20 mM MES (pH 6.0), 0.2 mM MgCl<sub>2</sub>, 1 mM EGTA, 1.5 mM PMSF, 1× protease inhibitor cocktail, 5 mM DTT). The lysate was sonicated at 30% amplitude in 30-s on-off cycles for 3 min, followed by the immediate addition of 500 mM NaCl. The lysate was boiled for 15 min and centrifuged at 15 000 × g for 1 h. Supernatants were purified using Ni-NTA resin (Qiagen # 30210). The bound resin was washed with wash buffer (50 mM phosphate buffer (pH 7.2), 200 mM NaCl, 20 mM imidazole) and eluted with elution buffer (50 mM phosphate buffer (pH 7.2), 200 mM NaCl, 500 mM imidazole). TEV protease purified in-house from a TEV expression plasmid obtained from Addgene (#135464) was then added to remove the His-tag, and the solution was incubated overnight at 4 °C. To further purify the protein, ion exchange chromatography (Bio-Rad #1580030) was performed to remove dimers and other undesired proteins. The protein elutes were concentrated using a protein concentrator (Sartorius #VS15T01). Phosphorylation of wild-type tau was performed *in vitro* following Abasi et al.<sup>25</sup>. A total of 100 μM tau was incubated with 2 μL PKA (New England BioLabs #P6000S) in kinase buffer containing 20 mM HEPES (pH 7.2), 50 mM NaCl, 0.5 mM TCEP, 4 mM adenosine-5'-triphosphate (Sigma #A7699-5G), 1 mM PMSF and 10 mM MgCl<sub>2</sub> at 30 °C for 16 h. To inactivate the kinase, the mixture was incubated at 65 °C for 20 min. Subsequently, buffer exchange was performed using a 30 kDa-cutoff Amicon centrifugal filter to replace the kinase buffer with 50 mM HEPES and 25 mM NaCl. Phosphorylation results were verified by SDS-PAGE mobility shift and LC-MS/MS analysis (methods in Supplementary Methods). For protein labeling, the purified protein was mixed with a 10-fold molar excess of Cy5-maleimide (Cytiva #25800674) and incubated for 2 h at room temperature (RT) in reaction buffer (50 mM phosphate buffer, 0.05 mM TCEP). Free dye was removed by gel filtration (Bio-Rad #1500738). The Cy5-labeled tau proteins were then concentrated using a protein concentrator (Sartorius #VS15T01).

### Single-molecule imaging

To prepare DNA constructs for surface attachment, λ-DNA (Thermo #SD0021) was linearized by ligating 5'- and 3'-biotinylated oligonucleotides targeting the cohesive ends at a 100× molar excess in 1× NEB ligase buffer for 5 min at 65 °C (the full list of oligonucleotides used in this study is provided in Supplementary Data 1). The mixture was then slowly cooled over 3 h. T4 DNA ligase (NEB #M0202L) and 1 mM ATP were added, followed by overnight ligation. The sample was purified using a 100 kDa cutoff buffer exchange filter (Merck, #UFC510024) to remove free primers and exchange the buffer for distilled water. A flow chamber for imaging was constructed using previously described methods<sup>98,99</sup>. In brief, two PEGylated glass coverslips were assembled with double-sided adhesive spacers to create a narrow flow channel. The coverslips were PEGylated through a first round using a 99:1 mixture of 5-kDa mPEG and biotin-PEG (Laysan Bio, #BIO-PEG-SVA-5K-100MG & MPEG-SVA-5K-1g), the coverslips were subjected to a second round of overnight PEGylation with a solution of 2-kDa mPEG (Laysan Bio #MPEG-SVA-2000-1g) without biotin-PEG to ensure optimal passivation. Before imaging, sample solutions were introduced into the

chamber using a syringe pump. For capturing DNA samples, 8 nM NeutrAvidin (Thermo #31000) was introduced into the flow cell, incubated for 5 min, and then washed with PBS. The flow cell surface was further passivated by infusing 5% BSA (Sigma #A0100-010) for 10 min, followed by another PBS wash. Biotinylated λ-DNA was diluted to 10–20 pM, injected, and immobilized on the surface for 7 min. For imaging, the buffer was exchanged with 200 μL of imaging buffer (50 mM HEPES (pH 7.1), 100 mM NaCl, 2 mM Trolox, 59.5 nM protocatechuate 3,4-dioxygenase (PCD #P8279-25UN), and 2.5 mM protocatechuic acid (PCA #37580-25G-F)) containing 20 nM SYTOX Orange (Thermo #S11368) and incubated for 10 min. To examine tau–DNA co-condensation, tau protein was diluted in the imaging buffer to concentrations ranging from 50 nM to 5 μM and then injected into the flow cell. All images were taken on a home-built objective-type TIRF microscopy setup. Samples were illuminated with 488 nm, 532 nm, and 633 nm CW lasers (Cobolt) and imaged through a 60× oil-immersion lens (Olympus, NA 1.49 for TIRF microscopy) onto a high-sensitivity sCMOS camera (Photometrics Prime BSI Express). Images were acquired typically at 108-nm spatial resolution with 100-ms exposure time using custom LabVIEW software. When necessary, fluorescence in two channels was separated by a dual-view image splitter (Cairn OptoSplit II) and recorded simultaneously. Additional methods for characterizing tau–DNA co-condensation, image analysis, including mobility shift and bulk LLPS assays, FRAP, DNA skybridge experiments, and nucleosome reconstitution and verification (Supplementary Note 2) are described in the Supplementary Information.

### Single-particle tracking

Tracking of tau condensates on DNA was performed by analyzing movies from DNA skybridge experiments using custom MATLAB scripts. After registering the tau and DNA fluorescence channels, tau particles were detected by intensity thresholding, and only those colocalizing with DNA foci were included in the diffusion analysis. Additionally, to avoid surface artifacts the skybridge substrates, particles within 7 pixels of the ridges or adhered to the bottom surface were excluded from analysis. Mean-squared displacements (MSD) were calculated as a function of time lag  $\Delta t$  and fit to  $MSD(\Delta t) = 2D(\Delta t)^\alpha$  to extract the diffusion coefficient  $D$  and anomalous exponent  $\alpha$ .

### Magnetic tweezers experiments

The preparation of the 10-kb dsDNA construct used in this work is detailed in our previous work<sup>40</sup>. Briefly, three DNA fragments were generated by PCR from λ-DNA: one 10 kb fragment and two 500 bp fragments (the list of primers is provided in Supplementary Data 1). During PCR, the 500 bp fragments were labeled with multiple biotin or digoxigenin molecules by incorporating biotin- or digoxigenin-labeled dUTP (Sigma, #11093070910, #11093088910). All three PCR products were digested with BsaI (NEB, #R3733S) for 4 h at 37 °C, and after cleanup, were ligated overnight using T4 DNA ligase (NEB, #M0202L) at RT. The ligated product was then purified by agarose gel electrophoresis. Details of the flow cell construction, sample assembly, and the home-built magnetic tweezers setup are available in our previous work<sup>100,101</sup>. Briefly, the magnetic tweezers consisted of a pair of permanent magnets positioned above the flow cell on an inverted microscope, allowing controlled application of force to paramagnetic beads tethered to single DNA molecules. For measurements, the DNA samples were injected into the flow cell so that the biotinylated ends could attach to PEGylated glass surfaces via biotin-avidin interactions, while the digoxigenin-labeled ends were coupled to anti-digoxigenin-coated magnetic beads (Sigma, #11333089001, Invitrogen, #M-270), which were injected afterward. To apply force, an antiparallel pair of cubic neodymium magnets (N52, 3/8") was placed above the flow cell, with a 1-mm gap between the magnets. The height and rotation of the magnets were controlled using a translation stage (PI, #L-40620DD10) and a stepper motor. Magnetic beads were illuminated with a 680 nm

super-luminescent diode and imaged using a 100× objective lens (Olympus, #UPLXAPO100XO) with a high-speed CMOS camera (Mikrotron, #EoSens 3CXP). Before measurements, the integrity of the dsDNA constructs (*i.e.*, the absence of nicks) was checked by rotating the samples and observing supercoiling behavior (Supplementary Fig. 7). When necessary, the force-extension curves were corrected for the off-axis tilting of magnetic beads<sup>102</sup>. For fluorescence verification, DNA-bound tau protein labeled with Cy3 was imaged simultaneously with magnetic tweezing using a 532 nm laser aligned for TIRF illumination and an sCMOS camera (Photometrics, #Prime BSI Express)<sup>40</sup>. All measurements were conducted in a buffer containing 50 mM HEPES (pH 7.1), 100 mM NaCl, 59.5 nM PCD, 2.5 mM PCA, and 0.1% BSA.

### Molecular dynamics simulation

Tau and DNA were coarse-grained as 3.4 nm beads and simulated via Langevin dynamics in HOOMD-blue (see Supplementary Note 1 for more details). A 10 kb DNA strand was represented by 1000 beads connected by harmonic springs and an angular potential set to yield a 150 bp persistence length; tau was modeled using identical beads with short-range attractive interactions to DNA and to itself. Interaction parameters were calibrated so that tau phase separation occurred only in the presence of DNA, and control simulations were conducted with DNA bending rigidity removed. Simulations comprised two phases: first, DNA ends were held at 50% extension while the tau–DNA co-condensate was allowed to assemble and equilibrate; second, a constant force was applied to one DNA terminus, with the opposite end fixed, to probe the mechanical response of the stabilized co-condensate.

### Microtubule capture assay

Tau protein was diluted to 5 μM in imaging buffer (same as above) supplemented with 5% 10 kDa PEG, and then slowly injected into a sample with biotinylated λ-DNA to form condensates. After co-condensate formation, HiLyte 488-labeled tubulin (Cytoskeleton, #TL488M-A) was mixed with unlabeled tubulin (Cytoskeleton, #T240-B), making up 4% of the total tubulin concentration. The mixture was prepared in imaging buffer supplemented with 1 mM GTP and 5% 10-kDa PEG to achieve a final tubulin concentration of 5–10 μM, while maintaining the tau concentration from the co-condensation experiments. After microtubule polymerization, the solution was slowly injected (7 μL min<sup>-1</sup>) into the chamber, with or without tau–DNA co-condensates. The assay with 12×601 DNA (naked and nucleosomal) was identical to the above protocol except for three changes: (1) the flow chamber was additionally blocked with 5% (w/v) BSA for 15 min; (2) after blocking, buffers were switched to HEPES/NaCl instead of PBS; and (3) the fluorophore set was changed to Alexa 488 (Sigma, #A10254 1 mg)–H2A (nucleosomes), Cy3(Cytiva #25800673)–tau, and HiLyte 647–tubulin (Cytoskeleton, #TL670M-A).

### Immunofluorescence imaging

For mammalian expression of mCherry-tagged tau variants, tau inserts were PCR-amplified from the bacterial plasmid and inserted into a mammalian expression vector (pmCherry-C1) by Gibson assembly. HEK-293 cells (Korean cell line bank, #21573) were then reverse-transfected with the appropriate tau plasmids using polyethyleneimine (Sigma, #P3143). A total of 2.5×10<sup>5</sup> HEK-293 cells were seeded onto 35 mm glass-bottom confocal dishes (SPL, #210350) with 2 μg mL<sup>-1</sup> mCherry–Tau plasmids and 4 μg mL<sup>-1</sup> polyethyleneimine (PEI, #P3143-100ML) in DMEM (Sigma #D6429) supplemented with 10% FBS (Welgene, #S101), and incubated for 36 h. For SH-SY5Y cells (Korean cell line bank, #22266), 1×10<sup>6</sup> cells were seeded onto the same dishes in RPMI-1640 (Sigma #R8758-500ML) supplemented with 10% FBS and were incubated for 24 h. To synchronize the cells, they were treated with 2 mM thymidine (Sigma, #T9250) for 16 h to induce the first synchronization block, then released into their respective media (with 10% FBS) for 8 h. This was followed by a second 16 h thymidine

block. After the second block, the cells were washed with PBS and released into their specific media with 10% FBS. Cells in the M phase were collected 9 h after release. The cells were then fixed with ice-cold methanol for 10 min, permeabilized with 0.25% Triton X-100 (Sigma, #X100) in PBS for 15 min, and blocked with 5% BSA in PBS with 0.05% Tween-20 (Sigma, #P1379) (PBST) for 1 h at RT. The full list of antibodies for staining is provided in the Supplementary Materials. Primary antibodies were diluted in PBST and incubated for 1 h at RT or overnight at 4 °C. After washing in PBST, cells were incubated with secondary antibodies diluted in PBST for 1 h at RT. After antibody staining, the cells were washed in PBST and incubated with 1 mg mL<sup>-1</sup> Hoechst 33258 (Sigma, #B2883-25mg) diluted 1:1,000 in PBST for 10 min at RT. Following a final wash in PBS, coverslips were mounted on confocal dishes using mounting solution (Agilent, #S203280-2). Finally, the cells were imaged using a Zeiss LSM 900 confocal microscope equipped with Airyscan 2. Details of image analysis procedures and western blot methods (including antibodies) are provided in the Supplementary Materials.

### RNA sequencing and analysis

RNA was extracted from mCherry–Tau-expressing HEK-293 cells and untreated HEK-293 cells for control. The extracted RNA was purified and sequenced using the NovaSeqX platform at Macrogen (Seoul, Korea). Paired-end raw sequencing reads were pre-processed with FastQC and trimmed using Trimmomatic-0.39. The cDNA reads were aligned with HISAT2.1, and differential expression was defined and quantified using the DESeq program with criteria of log<sub>2</sub> fold change > 0.7 or < -0.7, along with *p* values < 0.05. To identify biological pathways associated with the differentially expressed genes, ShinyGO 0.80 was used for analysis with the Gene Ontology (GO) database. For the heatmap, log<sub>2</sub> fold changes of genes corresponding to specific pathways were plotted, and a Venn diagram was generated for pathways involving downregulated genes.

### Reporting summary

Further information on research design is available in the Nature Portfolio Reporting Summary linked to this article.

### Data availability

The RNA sequencing data are publicly available via NCBI BioProject accession number PRJNA1173100 ([https://www.ncbi.nlm.nih.gov/sra/SRX26385062\[accn\]](https://www.ncbi.nlm.nih.gov/sra/SRX26385062[accn])). Source data are provided as a Source Data file. All additional raw data files, including TIRF/confocal micrographs, are available from the corresponding author on request. Source data are provided with this paper.

### Code availability

The code used for data analysis is available both at Github (<https://github.com/ShonLab>) and Zenodo (<https://doi.org/10.5281/zenodo.17797566>).

### References

- Weingarten, M. D., Lockwood, A. H., Hwo, S. Y. & Kirschner, M. W. A protein factor essential for microtubule assembly. *Proc. Natl. Acad. Sci.* **72**, 1858–1862 (1975).
- Kadavath, H. et al. Tau stabilizes microtubules by binding at the interface between tubulin heterodimers. *Proc. Natl. Acad. Sci.* **112**, 7501–7506 (2015).
- Hernández-Vega, A. et al. Local nucleation of microtubule bundles through tubulin concentration into a condensed tau phase. *Cell Rep.* **20**, 2304–2312 (2017).
- Zhang, X. et al. RNA stores tau reversibly in complex coacervates. *PLoS Biol.* **15**, e2002183 (2017).
- Ambadipudi, S., Biernat, J., Riedel, D., Mandelkow, E. & Zweckstetter, M. Liquid–liquid phase separation of the microtubule-

- binding repeats of the Alzheimer-related protein Tau. *Nat. Commun.* **8**, 275 (2017).
6. Wegmann, S. et al. Tau protein liquid–liquid phase separation can initiate tau aggregation. *EMBO J.* **37**, e98049 (2018).
  7. Lee-Eom, C., Jung, J., Park, C. & Shon, M. J. Structural role of Tau-Tubulin co-condensates in early microtubule organization. Preprint at <https://doi.org/10.1101/2024.11.04.621946> (2024).
  8. Boeynaems, S. et al. Protein phase separation: a new phase in cell biology. *Trends Cell Biol.* **28**, 420–435 (2018).
  9. Shin, Y. & Brangwynne, C. P. Liquid phase condensation in cell physiology and disease. *Science* **357**, eaaf4382 (2017).
  10. Wang, Y. & Mandelkow, E. Tau in physiology and pathology. *Nat. Rev. Neurosci.* **17**, 22–35 (2016).
  11. Rai, S. K., Savastano, A., Singh, P., Mukhopadhyay, S. & Zweckstetter, M. Liquid–liquid phase separation of tau: From molecular biophysics to physiology and disease. *Protein Sci.* **30**, 1294–1314 (2021).
  12. Mukrasch, M. D. et al. Structural polymorphism of 441-residue tau at single residue resolution. *PLOS Biol.* **7**, e1000034 (2009).
  13. Lin, Y. et al. Narrow equilibrium window for complex coacervation of tau and RNA under cellular conditions. *eLife* **8**, e42571 (2019).
  14. Ash, P. E. A. et al. TIA1 potentiates tau phase separation and promotes generation of toxic oligomeric tau. *Proc. Natl. Acad. Sci.* **118**, e2014188118 (2021).
  15. Kampers, T., Friedhoff, P., Biernat, J., Mandelkow, E.-M. & Mandelkow, E. RNA stimulates aggregation of microtubule-associated protein tau into Alzheimer-like paired helical filaments. *FEBS Lett.* **399**, 344–349 (1996).
  16. Lin, Y. et al. Liquid-liquid phase separation of tau driven by hydrophobic interaction facilitates fibrillization of Tau. *J. Mol. Biol.* **433**, 166731 (2021).
  17. Hochmair, J. et al. Molecular crowding and RNA synergize to promote phase separation, microtubule interaction, and seeding of Tau condensates. *EMBO J.* **41**, e108882 (2022).
  18. Wiche, G., Corces, V. G. & Avila, J. Preferential binding of hog brain microtubule-associated proteins to mouse satellite versus bulk DNA preparations. *Nature* **273**, 403–405 (1978).
  19. Hua, Q. et al. Microtubule associated protein tau binds to double-stranded but not single-stranded DNA. *Cell. Mol. Life Sci. CMLS* **60**, 413–421 (2003).
  20. Qu, M. et al. Neuronal tau induces DNA conformational changes observed by atomic force microscopy. *NeuroReport* **15**, 2723 (2004).
  21. Wei, Y. et al. Binding to the minor groove of the double-strand, tau protein prevents DNA from damage by peroxidation. *PLOS ONE* **3**, e2600 (2008).
  22. Camero, S. et al. Thermodynamics of the Interaction between Alzheimer’s Disease Related Tau Protein and DNA. *PLOS ONE* **9**, e104690 (2014).
  23. Camero, S. et al. Tau protein provides DNA with Thermodynamic and structural features which are similar to those found in histone-DNA complex. *J. Alzheimers Dis.* **39**, 649–660 (2014).
  24. Qi, H. et al. Nuclear magnetic resonance spectroscopy characterization of interaction of tau with DNA and its regulation by phosphorylation. *Biochemistry* **54**, 1525–1533 (2015).
  25. Abasi, L. S. et al. Phosphorylation regulates tau’s phase separation behavior and interactions with chromatin. *Commun. Biol.* **7**, 1–17 (2024).
  26. Sultan, A. et al. Nuclear Tau, a Key Player in Neuronal DNA Protection\*. *J. Biol. Chem.* **286**, 4566–4575 (2011).
  27. Bukar Maina, M., Al-Hilaly, Y. K. & Serpell, L. C. Nuclear Tau and Its Potential Role in Alzheimer’s Disease. *Biomolecules* **6**, 9 (2016).
  28. Antón-Fernández, A., Vallés-Saiz, L., Avila, J. & Hernández, F. Neuronal nuclear tau and neurodegeneration. *Neuroscience* **518**, 178–184 (2023).
  29. Kirschner, M. & Mitchison, T. Beyond self-assembly: From microtubules to morphogenesis. *Cell* **45**, 329–342 (1986).
  30. Kanaan, N. M., Hamel, C., Grabinski, T. & Combs, B. Liquid-liquid phase separation induces pathogenic tau conformations in vitro. *Nat. Commun.* **11**, 2809 (2020).
  31. Larson, A. G. et al. Liquid droplet formation by HP1 $\alpha$  suggests a role for phase separation in heterochromatin. *Nature* **547**, 236–240 (2017).
  32. Shin, Y. et al. Liquid nuclear condensates mechanically sense and restructure the genome. *Cell* **175**, 1481–1491.e13 (2018).
  33. Quail, T. et al. Force generation by protein–DNA co-condensation. *Nat. Phys.* **17**, 1007–1012 (2021).
  34. Bell, N. A. W. et al. Single-molecule measurements reveal that PARP1 condenses DNA by loop stabilization. *Sci. Adv.* **7**, eabf3641 (2021).
  35. Nguyen, T. et al. Chromatin sequesters pioneer transcription factor Sox2 from exerting force on DNA. *Nat. Commun.* **13**, 3988 (2022).
  36. Renger, R. et al. Co-condensation of proteins with single- and double-stranded DNA. *Proc. Natl. Acad. Sci.* **119**, e2107871119 (2022).
  37. Chappidi, N. et al. PARP1-DNA co-condensation drives DNA repair site assembly to prevent disjunction of broken DNA ends. *Cell* **187**, 945–961.e18 (2024).
  38. Kim, D. et al. DNA skybridge: 3D structure producing a light sheet for high-throughput single-molecule imaging. *Nucleic Acids Res* **47**, e107 (2019).
  39. Sjöberg, M. K., Shestakova, E., Mansuroglu, Z., Maccioni, R. B. & Bonnefoy, E. Tau protein binds to pericentromeric DNA: a putative role for nuclear tau in nucleolar organization. *J. Cell Sci.* **119**, 2025–2034 (2006).
  40. Jung, J., Kim, S., Rah, S.-H., Lee, J. & Shon, M. J. Chapter Five - Force-fluorescence setup for observing protein–DNA interactions under load. in *Methods in Enzymology* (eds Ju Shon, M. & Yoon, T.-Y.) **694**, 137–165 (Academic Press, 2024).
  41. Pavin, N. & Tolić-Nørrelykke, I. M. Swinging a sword: how microtubules search for their targets. *Syst. Synth. Biol.* **8**, 179–186 (2014).
  42. Buée, L., Bussièrè, T., Buée-Scherrer, V., Delacourte, A. & Hof, P. R. Tau protein isoforms, phosphorylation and role in neurodegenerative disorders1. *Brain Res. Rev.* **33**, 95–130 (2000).
  43. Köpke, E. et al. Microtubule-associated protein tau. Abnormal phosphorylation of a non-paired helical filament pool in Alzheimer’s disease. *J. Biol. Chem.* **268**, 24374–24384 (1993).
  44. Liu, F. et al. PKA modulates GSK-3 $\beta$ - and cdk5-catalyzed phosphorylation of tau in site- and kinase-specific manners. *FEBS Lett.* **580**, 6269–6274 (2006).
  45. Scott, C. W. et al. Phosphorylation of recombinant tau by cAMP-dependent protein kinase. Identification of phosphorylation sites and effect on microtubule assembly. *J. Biol. Chem.* **268**, 1166–1173 (1993).
  46. Mansuroglu, Z. et al. Loss of Tau protein affects the structure, transcription and repair of neuronal pericentromeric heterochromatin. *Sci. Rep.* **6**, 33047 (2016).
  47. Wegmann, S., Biernat, J. & Mandelkow, E. A current view on Tau protein phosphorylation in Alzheimer’s disease. *Curr. Opin. Neurobiol.* **69**, 131–138 (2021).
  48. Hasegawa, M. et al. Protein sequence and mass spectrometric analyses of tau in the Alzheimer’s disease brain. *J. Biol. Chem.* **267**, 17047–17054 (1992).
  49. Biernat, J., Gustke, N., Drewes, G., Mandelkow, E. - & Mandelkow, E. Phosphorylation of Ser262 strongly reduces binding of tau to

- microtubules: Distinction between PHF-like immunoreactivity and microtubule binding. *Neuron* **11**, 153–163 (1993).
50. Sengupta, A. et al. Phosphorylation of Tau at Both Thr 231 and Ser 262 Is Required for Maximal Inhibition of Its Binding to Microtubules. *Arch. Biochem. Biophys.* **357**, 299–309 (1998).
51. Wesseling, H. et al. Tau PTM profiles identify patient heterogeneity and stages of Alzheimer's disease. *Cell* **183**, 1699–1713.e13 (2020).
52. Léger, J., Kempf, M., Lee, G. & Brandt, R. Conversion of serine to aspartate imitates phosphorylation-induced changes in the structure and function of microtubule-associated Protein Tau \*. *J. Biol. Chem.* **272**, 8441–8446 (1997).
53. Alonso, A. D. et al. Phosphorylation of Tau at Thr212, Thr231, and Ser262 Combined Causes Neurodegeneration \*. *J. Biol. Chem.* **285**, 30851–30860 (2010).
54. Song, L., Oseid, D. E., Wells, E. A. & Robinson, A. S. The Interplay between GSK3 $\beta$  and Tau Ser262 Phosphorylation during the Progression of Tau Pathology. *Int. J. Mol. Sci.* **23**, 11610 (2022).
55. Boyko, S. & Surewicz, W. K. Domain-specific modulatory effects of phosphomimetic substitutions on liquid-liquid phase separation of tau protein. *J. Biol. Chem.* **299**, 104722 (2023).
56. Boyko, S., Qi, X., Chen, T.-H., Surewicz, K. & Surewicz, W. K. Liquid-liquid phase separation of tau protein: The crucial role of electrostatic interactions. *J. Biol. Chem.* **294**, 11054–11059 (2019).
57. Su, X. et al. Phase separation of signaling molecules promotes T cell receptor signal transduction. *Science* **352**, 595–599 (2016).
58. Binder, L. I., Frankfurter, A. & Rebhun, L. I. The distribution of tau in the mammalian central nervous system. *J. Cell Biol.* **101**, 1371–1378 (1985).
59. Khatoun, S., Grundke-Iqbal, I. & Iqbal, K. Brain levels of microtubule-associated protein  $\tau$  are elevated in alzheimer's disease: a radioimmuno-slot-blot assay for nanograms of the protein. *J. Neurochem.* **59**, 750–753 (1992).
60. Kanaan, N. M. & Grabinski, T. Neuronal and glial distribution of tau protein in the adult rat and monkey. *Front. Mol. Neurosci.* **14**, 607303 (2021).
61. Greenwood, J. A. & Johnson, G. V. W. Localization and in Situ Phosphorylation State of Nuclear Tau. *Exp. Cell Res.* **220**, 332–337 (1995).
62. Gouveia, B. et al. Capillary forces generated by biomolecular condensates. *Nature* **609**, 255–264 (2022).
63. Setru, S. U. et al. A hydrodynamic instability drives protein droplet formation on microtubules to nucleate branches. *Nat. Phys.* **17**, 493–498 (2021).
64. Frost, B., Hemberg, M., Lewis, J. & Feany, M. B. Tau promotes neurodegeneration through global chromatin relaxation. *Nat. Neurosci.* **17**, 357–366 (2014).
65. Rico, T. et al. Tau stabilizes chromatin compaction. *Front. Cell Dev. Biol.* **9**, (2021).
66. Roulland, Y. et al. The flexible ends of CENP-a nucleosome are required for mitotic fidelity. *Mol. Cell* **63**, 674–685 (2016).
67. Alquezar, C., Arya, S. & Kao, A. W. Tau post-translational modifications: dynamic transformers of tau function, degradation, and aggregation. *Front. Neurol.* **11**, 595532 (2021).
68. Baumann, K., Mandelkow, E.-M., Biernat, J., Piwnicka-Worms, H. & Mandelkow, E. Abnormal Alzheimer-like phosphorylation of tau-protein by cyclin-dependent kinases cdk2 and cdk5. *FEBS Lett.* **336**, 417–424 (1993).
69. Illenberger, S. et al. The endogenous and cell cycle-dependent phosphorylation of tau protein in living cells: implications for alzheimer's disease. *Mol. Biol. Cell* **9**, 1495–1512 (1998).
70. Hamdane, M. et al. Mitotic-like tau phosphorylation by p25-Cdk5 kinase complex \*. *J. Biol. Chem.* **278**, 34026–34034 (2003).
71. Flores-Rodríguez, P. et al. Phospho-tau protein expression in the cell cycle of SH-SY5Y neuroblastoma cells: a morphological study. *J. Alzheimers Dis.* **71**, 631–645 (2019).
72. Itoh, G. et al. Lateral attachment of kinetochores to microtubules is enriched in prometaphase rosette and facilitates chromosome alignment and bi-orientation establishment. *Sci. Rep.* **8**, 3888 (2018).
73. Tanaka, K. Regulatory mechanisms of kinetochore-microtubule interaction in mitosis. *Cell. Mol. Life Sci.* **70**, 559–579 (2013).
74. Villasante, A., Corces, V. G., Manso-Martínez, R. & Avila, J. Binding of microtubule protein to DNA and chromatin: possibility of simultaneous linkage of microtubule to nucleic acid and assembly of the microtubule structure. *Nucleic Acids Res* **9**, 895–908 (1981).
75. Wollman, R. et al. Efficient chromosome capture requires a bias in the 'search-and-capture' process during mitotic-spindle assembly. *Curr. Biol.* **15**, 828–832 (2005).
76. David, A. F. et al. Augmin accumulation on long-lived microtubules drives amplification and kinetochore-directed growth. *J. Cell Biol.* **218**, 2150–2168 (2019).
77. Renda, F. et al. Non-centrosomal microtubules at kinetochores promote rapid chromosome biorientation during mitosis in human cells. *Curr. Biol.* **32**, 1049–1063.e4 (2022).
78. Houck, A. L., Hernández, F. & Ávila, J. A simple model to study tau pathology. *J. Exp. Neurosci.* **10**, S25100 (2016). JEN.
79. Bougé, A.-L. & Parmentier, M.-L. Tau excess impairs mitosis and kinesin-5 function, leading to aneuploidy and cell death. *Dis. Model. Mech.* **9**, 307–319 (2016).
80. Malmanche, N. et al. Developmental expression of 4-repeat-tau induces neuronal aneuploidy in Drosophila tauopathy models. *Sci. Rep.* **7**, 40764 (2017).
81. Rossi, G. et al. A new function of microtubule-associated protein tau: Involvement in chromosome stability. *Cell Cycle* **7**, 1788–1794 (2008).
82. Violet, M. et al. A major role for Tau in neuronal DNA and RNA protection in vivo under physiological and hyperthermic conditions. *Front. Cell. Neurosci.* **8**, 84 (2014).
83. Mueller, R. L. et al. Tau: a signaling hub protein. *Front. Mol. Neurosci.* **14**, 647054 (2021).
84. Andorfer, C. et al. Cell-Cycle Reentry and Cell Death in Transgenic Mice Expressing Nonmutant Human Tau Isoforms. *J. Neurosci.* **25**, 5446–5454 (2005).
85. Koseoglu, M. M., Norambuena, A., Sharlow, E. R., Lazo, J. S. & Bloom, G. S. Aberrant Neuronal Cell Cycle Re-Entry: The Pathological Confluence of Alzheimer's Disease and Brain Insulin Resistance, and Its Relation to Cancer. *J. Alzheimers Dis.* **67**, 1–11 (2019).
86. Frost, B. Alzheimer's disease and related tauopathies: disorders of disrupted neuronal identity. *Trends Neurosci.* **46**, 797–813 (2023).
87. Mu, Y. & Gage, F. H. Adult hippocampal neurogenesis and its role in Alzheimer's disease. *Mol. Neurodegener.* **6**, 85 (2011).
88. Salta, E. et al. Adult hippocampal neurogenesis in Alzheimer's disease: a roadmap to clinical relevance. *Cell Stem Cell* **30**, 120–136 (2023).
89. Grundke-Iqbal, I. et al. Abnormal phosphorylation of the microtubule-associated protein tau ( $\tau$ ) in Alzheimer's cytoskeletal pathology. *Proc. Natl. Acad. Sci.* **83**, 4913–4917 (1986).
90. Alonso, A. et al. Hyperphosphorylation induces self-assembly of  $\tau$  into tangles of paired helical filaments/straight filaments. *Proc. Natl. Acad. Sci.* **98**, 6923–6928 (2001).
91. Schroeder, C. et al. Aberrant expression of the microtubule-associated protein tau is an independent prognostic feature in prostate cancer. *BMC Cancer* **19**, 193 (2019).
92. Gargini, R., Segura-Collar, B. & Sánchez-Gómez, P. Novel functions of the neurodegenerative-related gene tau in cancer. *Front. Aging Neurosci.* **11**, 231 (2019).

93. Clementi, L. et al. Mitotic phosphorylation of Tau/MAPT modulates cell cycle progression in prostate cancer cells. *J. Cancer Res. Clin. Oncol.* **149**, 7689–7701 (2023).
94. Koo, D.-H. et al. Tau and PTEN status as predictive markers for response to trastuzumab and paclitaxel in patients with HER2-positive breast cancer. *Tumor Biol.* **36**, 5865–5871 (2015).
95. Derisbourg, M. et al. Role of the Tau N-terminal region in microtubule stabilization revealed by new endogenous truncated forms. *Sci. Rep.* **5**, 9659 (2015).
96. Boyko, S., Surewicz, K. & Surewicz, W. K. Regulatory mechanisms of tau protein fibrillation under the conditions of liquid–liquid phase separation. *Proc. Natl. Acad. Sci.* **117**, 31882–31890 (2020).
97. Dujardin, S. et al. Tau molecular diversity contributes to clinical heterogeneity in Alzheimer’s disease. *Nat. Med.* **26**, 1256–1263 (2020).
98. Lee, H.-W. et al. Profiling of protein–protein interactions via single-molecule techniques predicts the dependence of cancers on growth-factor receptors. *Nat. Biomed. Eng.* **2**, 239–253 (2018).
99. Cha, M. et al. Quantitative imaging of vesicle–protein interactions reveals close cooperation among proteins. *J. Extracell. Vesicles* **12**, 12322 (2023).
100. Park, C. et al. High-speed magnetic tweezers for nanomechanical measurements on force-sensitive elements. *J. Vis. Exp.* <https://doi.org/10.3791/65137> (2023).
101. Hong, S. et al. *High-speed measurements of SNARE–complexin interactions using magnetic tweezers*. in *Methods in Enzymology*, Chapter Four, (eds Ju Shon, M. & Yoon, T.-Y.) **694**, 109–135 (Academic Press, 2024).
102. Shon, M. J., Rah, S.-H. & Yoon, T.-Y. Submicrometer elasticity of double-stranded DNA revealed by precision force-extension measurements with magnetic tweezers. *Sci. Adv.* **5**, eaav1697 (2019).
- prepared all samples. C.P. performed TIRF imaging and microtubule experiments. J.J., J.Y.B., and S.-H.R. performed magnetic tweezers experiments. J.J. and H.Y. conducted confocal imaging and bulk LLPS experiments. K.Y. conducted skybridge experiments, and J.S. analyzed the results. A.J. and S.H. performed RNA sequencing and analysis. M.K. with C.L. ran tau–DNA binding simulations and analyzed the results, and J.-H.J. oversaw data analysis. M.J.S., D.S.H., J.-B.L., J.-H.J., and Y.K. supervised the study. C.P., J.J., H.Y., J.S., S.H., K.Y., M.K., and C.L. prepared figures and drafted the initial manuscript. M.J.S., C.P., and J.J. wrote and edited the final manuscript with contributions from all authors.

## Competing interests

The authors declare no competing interests.

## Additional information

**Supplementary information** The online version contains supplementary material available at <https://doi.org/10.1038/s41467-025-67888-x>.

**Correspondence** and requests for materials should be addressed to Dong Soo Hwang or Min Ju Shon.

**Peer review information** *Nature Communications* thanks Paul Maddox, and the other anonymous, reviewer(s) for their contribution to the peer review of this work. A peer review file is available.

**Reprints and permissions information** is available at <http://www.nature.com/reprints>

**Publisher’s note** Springer Nature remains neutral with regard to jurisdictional claims in published maps and institutional affiliations.

**Open Access** This article is licensed under a Creative Commons Attribution-NonCommercial-NoDerivatives 4.0 International License, which permits any non-commercial use, sharing, distribution and reproduction in any medium or format, as long as you give appropriate credit to the original author(s) and the source, provide a link to the Creative Commons licence, and indicate if you modified the licensed material. You do not have permission under this licence to share adapted material derived from this article or parts of it. The images or other third party material in this article are included in the article’s Creative Commons licence, unless indicated otherwise in a credit line to the material. If material is not included in the article’s Creative Commons licence and your intended use is not permitted by statutory regulation or exceeds the permitted use, you will need to obtain permission directly from the copyright holder. To view a copy of this licence, visit <http://creativecommons.org/licenses/by-nc-nd/4.0/>.

© The Author(s) 2026

## Acknowledgements

We thank Jeong-Mo Choi, Cherlhyun Jeong, and Hajin Kim for helpful discussions; Euddeum E. Jeong, Gyu Ri Kim, Jiwon Jang, Sejoon Jeong, and Jong-Chan Lee for the help with cell imaging; Hee-Jung Jung for the help with mass spectrometry data analysis; Minkwon Cha, Sang-Hyeok Jeong, Surim Yoo, and Jiyoung Lee for the help with experiments; and the members of the Shon laboratory for discussions and assistance. We also thank UCRF (UNIST Central Research Facilities) for support in using the LC-MS/MS equipment; Gil-Yeol Ryu at the POSTECH Biotech Center for support with the Bio-TEM equipment. This work was supported by the National Research Foundation of Korea (NRF) grant funded by the Korea government (MSIT) (NRF-2022R1C1C1012176 and RS-2024-00344154 to M.J.S.; RS-2023-00218927 to J.-B.L., J.-H.J., M.J.S., and Y.K.; 2022R1C1C1005378 to Y.K.) and by POSTECH Basic Science Research Institute Grant (RS-2021-NR060139 to M.J.S.).

## Author contributions

M.J.S. conceived the project. C.P., J.J., Y.H., D.S.H., and M.J.S. designed the experiments. C.P., J.J., Y.H., H.Y., K.Y., J.Y.B., S.-H.R., C.L.-E., and M.S.

<sup>1</sup>Department of Physics, Pohang University of Science and Technology (POSTECH), Pohang, Republic of Korea. <sup>2</sup>School of Interdisciplinary Bioscience and Bioengineering, Pohang University of Science and Technology (POSTECH), Pohang, Republic of Korea. <sup>3</sup>Department of New Biology, Daegu Gyeongbuk Institute of Science and Technology (DGIST), Daegu, Republic of Korea. <sup>4</sup>New Biology Research Center, Daegu Gyeongbuk Institute of Science and Technology (DGIST), Daegu, Republic of Korea. <sup>5</sup>Division of Environmental Science and Engineering, Pohang University of Science and Technology (POSTECH), Pohang, Republic of Korea. <sup>6</sup>Present address: Max Planck Institute of Cell Biology and Genetics, Dresden, Germany. <sup>7</sup>These authors contributed equally: Celine Park, Jaehun Jung, Yuri Hong. ✉ e-mail: [dshwang@postech.ac.kr](mailto:dshwang@postech.ac.kr); [mjshon@postech.ac.kr](mailto:mjshon@postech.ac.kr)